Mon. Not. R. Astron. Soc. **000**, 1–18 (2002) Printed 15 May 2009 (MN LaTeX style file v2.2)

arXiv:0905.2512v1 [astro-ph.GA] 15 May 2009

Kinematics and history of the solar neighbourhood revisited

Michael Aumer[1]⋆ and James J. Binney[2]†
[1] *Universitätssternwarte München, Scheinerstr. 1, 81679 München, D*
[2] *Rudolf Peierls Centre for Theoretical Physics, University of Oxford, Oxford OX1 3NP, UK*

Accepted . Received ; in original form

ABSTRACT

We use proper motions and parallaxes from the new reduction of *Hipparcos* data and Geneva-Copenhagen radial velocities for a complete sample of $\sim 15\,000$ main-sequence and subgiant stars, and new Padova isochrones to constrain the kinematics and star-formation history of the solar neighbourhood. We rederive the solar motion and the structure of the local velocity ellipsoids. When the principal velocity dispersions are assumed to increase with time as t^{β}, the index β is larger for σ_W ($\beta_W \approx 0.45$) than for σ_U ($\beta_U \approx 0.31$). For the three-dimensional velocity dispersion we obtain $\beta = 0.35$. We exclude saturation of disc heating after $\sim 3\,\mathrm{Gyr}$ as proposed by Quillen & Garnett (2000). Saturation after $\gtrsim 4\,\mathrm{Gyr}$ combined with an abrupt increase in velocity dispersion for the oldest stars cannot be excluded. For all our models the star-formation rate is declining, being a factor 2–7 lower now than it was at the beginning. Models in which the SFR declines exponentially favour very high disc ages between 11.5 and 13 Gyr and exclude ages below $\sim 10.5\,\mathrm{Gyr}$ as they yield worse fits to the number density and velocity dispersion of red stars. Models in which the SFR is the sum of two declining exponentials representing the thin and thick discs favour ages between 10.5 and 12 Gyr with a lower limit of $\sim 10.0\,\mathrm{Gyr}$. Although in our models the star-formation rate peaked surprisingly early, the mean formation time of solar-neighbourhood stars is later than in ab-initio models of galaxy formation, probably on account of weaknesses in such models.

Key words: stars: kinematics - Galaxy: kinematics and dynamics - solar neighbourhood

1 INTRODUCTION

For the solar neighbourhood we have the most detailed observational data available for any galactic disc. In particular, the distributions within the solar neighbourhood of stellar ages, metallicities and space velocities are keys to deducing how the disc has evolved chemically and dynamically. Work directed at understanding how galaxies have formed and evolved is a major area of contemporary astronomy, and studies of the local disc have an important role to play in this effort. Despite much progress many questions about the evolution of the local disc remain open.

The *Hipparcos* catalogue provides uniquely useful data for studies of the solar neighbourhood, because the data are homogeneous and of high quality. Dehnen & Binney (1998, hereafter DB98) defined a kinematically unbiased sample of *Hipparcos* stars and investigated its kinematics, while Binney, Dehnen & Bertelli (2000, hereafter BDB00) used the sample to model the history of star formation and the stochastic acceleration of stars in the disc. In this paper we redefine the sample and then re-work these papers for several reasons.

(i) In a systematic re-reduction of the astrometric data from the *Hipparcos* satellite, van Leeuwen (2007) has been able to diminish significantly the errors for a large number of stars. Using the new data we can enlarge the sample of stars that can be used for modelling.

(ii) BDB00 did not take into account the variation of the scale height of stars with age. Consequently, their conclusions regarding past star-formation rates and rates of stochastic acceleration are wrong. Our analysis remedies this defect.

(iii) From an analysis of the age-velocity dispersion relation in the sample of 189 stars in Edvardsson et al. (1993), Quillen & Garnett (2000) argued that stochastic heating saturates after only 3 Gyr and that the velocity dispersion of disc stars increased abruptly $\sim 9\,\mathrm{Gyr}$ ago as a result of a

---

⋆ aumer@usm.lmu.de
† binney@thphys.ox.ac.uk

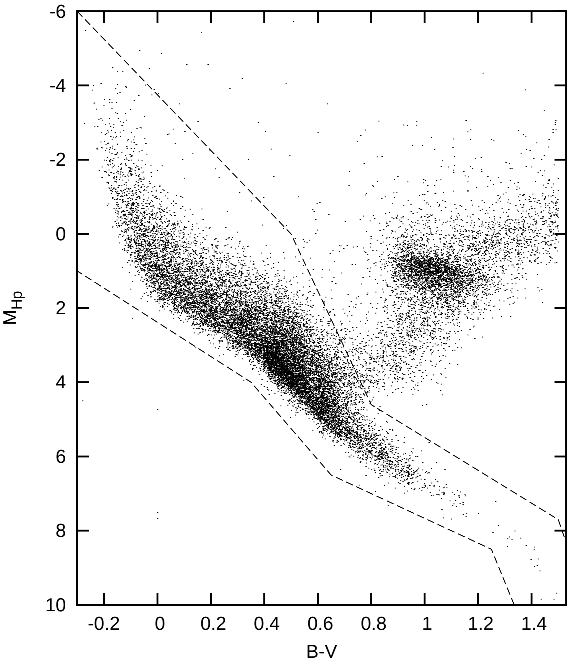

Figure 1. Colour-magnitude diagram of the magnitude limited subsample of 20 360 *Hipparcos* stars with relative parallax errors smaller than 10%. The lines indicate our selection of main-sequence stars, there are 15 113 stars between the lines

merger. We use our much larger sample to test this conjecture.

(iv) Metallicity and radial-velocity measurements from the Geneva Copenhagen Survey [Nordström et al. (2004), hereafter GCS, Holmberg et al. (2007), hereafter GCS2 and Holmberg et al. (2008), hereafter GCS3] of F and G dwarfs allow more accurate determinations of the metallicity distribution of disc stars and the three-dimensional velocity dispersions in the corresponding colour interval.

(v) New Padova isochrones have recently been published (Bertelli et al. 2008), allowing us to update the input concerning stellar evolution and to improve the modelling of the metallicity distribution.

(vi) A revision of the impact of interstellar reddening on our sample changes some results significantly.

The goal of this paper is the same as that of BDB00: to understand as much of the history of the disc as we can by modelling the large-scale structure of velocity space near the Sun. We do not address the small-scale structure of this space, which was first clearly revealed by the *Hipparcos* Catalogue through the work of Crezé et al. (1998) and Dehnen (1998).

Section 2 describes our input data. Section 3 updates DB98 by extracting the kinematics of the solar neighbourhood. The work of BDB00 is updated in Section 4, which describes our models, and Section 5, which describes fits of them to the data. Section 6 sums up and compares our results with those of other authors.

2 THE DATA

2.1 The Sample

We follow the procedure of DB98 to select from the new reduction of the *Hipparcos* catalogue (van Leeuwen 2007) a kinematically unbiased, magnitude-limited subsample of single stars with high-quality astrometric data.

We determine the apparent magnitude up to which the *Hipparcos* catalogue is complete ($V_{\rm lim} \approx 8\,$mag), which depends on colour and position on the sky, by comparing the *Hipparcos* catalogue with the *Tycho2* catalogue (Høg et al. 2000), which is complete to about $V_{\rm Tycho} = 11$. For $16\times16\times10$ uniformly spaced bins in galactic coordinates $\sin b$ and l and colour $(B-V)_{\rm Tycho}$ in $(-0.3, 1.5)$, we select those stars that are brighter than the second brightest star per bin that is in the *Tycho2* but not the *Hipparcos* catalogue. 44 567 out of the 118 218 *Hipparcos* stars are single stars that fulfil this criterion. From these stars we further select stars with relative parallax errors of 10% or less. This criterion reduces the sample from 44 567 to 20 360 but ensures that the measured proper motions yield fairly accurate tangential velocities.

Fig. 1 is the colour-magnitude diagram of the sample. For our analysis of the star-formation history, we require a one-to-one relationship between the maximum lifetime of a star and its colour, so we restrict ourselves to main-sequence stars. The lines within which stars are deemed to lie on the main sequence are shown in Fig. 1. The applied CMD cut leaves the possibility for a small number of subgiant stars to enter the sample in the colour range $0.6 < B-V < 0.75$, where the sample might thus be slightly biased towards old stars. The 15 113 stars that lie between these lines comprise our final sample, which is approximately 27% larger than that of DB98. The growth in the sample is most pronounced for blue stars since these tend to be more luminous and distant and therefore have the smallest parallaxes.

GCS have measured radial velocities for 6 918 single F and G dwarfs in our sample. These stars are confined to the colour interval $0.4 < B-V < 0.8$. We use this subsample, for which individual space velocities can be determined, as a control of the results obtained with the main sample.

2.2 Isochrones and Metallicities

The age distribution of main-sequence stars of a given colour must vary with colour because at the blue end of the main sequence all stars must be younger than the short main-sequence lifetime there, while at the red end of the main sequence we see stars that are as old as the disc in addition to recently-formed stars. We use Padova isochrones (Bertelli et al. 2008) for masses ranging from 0.15 to $4\,{\rm M}_\odot$ to determine the age distribution at each colour. Isochrones depend significantly on the metal content Z and the Helium abundance Y, so we have to use several isochrones to simulate the metallicity distribution of the solar neighbourhood. We refer to Section 5.1 for a discussion of the weightings of the isochrones employed and focus on which isochrones to employ.

For the conversion from solar units to Z and Y we need to know the solar abundances. Bertelli et al. (2008) argue that the update of the solar chemical composition

Table 1. The metallicities of the Padova isochrones that were used in the models and the corresponding [Fe/H] values, which were calculated with solar abundances $Z_\odot = 0.017$ and $Y_\odot = 0.260$.

Z	Y	[Fe/H]
0.002	0.23	−0.95
0.003	0.23	−0.78
0.004	0.23	−0.65
0.006	0.24	−0.47
0.008	0.24	−0.34
0.010	0.25	−0.24
0.012	0.25	−0.16
0.014	0.25	−0.09
0.017	0.26	0.00
0.020	0.27	0.08
0.026	0.28	0.20
0.036	0.30	0.36

by Grevesse et al. (2007) ($Y_\odot = 0.2486, Z_\odot = 0.0122$) gives rise to several problems and uncertainties and adopt ($Y_\odot = 0.260, Z_\odot = 0.017$) for their solar model. Moreover Chaplin et al. (2007) report that solar models with $Z < 0.0187$ are inconsistent with the helioseismic data. Since we use the Bertelli et al. (2008) isochrones, we use their solar composition.

As the measurement of the Helium abundance Y of a star is difficult, there is little data available on the relationship $Z(Y)$ within the solar neighbourhood. A common, but not undisputed procedure is to assume a linear enrichment law $Y = Y_\mathrm{p} + (\mathrm{d}Y/\mathrm{d}Z)Z$, where Y_p is the primordial helium abundance and $\mathrm{d}Y/\mathrm{d}Z$ is the helium-to-metal enrichment ratio. Jimenez et al. (2003) find $\mathrm{d}Y/\mathrm{d}Z = 2.1 \pm 0.4$ for $Y_\mathrm{p} = 0.236$, whereas Casagrande et al. (2007) using Padova isochrones find that it is doubtful whether a universal linear enrichment law exists. For metallicities similar to the solar one they also find $\mathrm{d}Y/\mathrm{d}Z = 2.1 \pm 0.9$. Unfortunately, this slope when combined with either the traditional values $(Y_\odot, Z_\odot) = (0.260, 0.017)$ or the new values $(0.2486, 0.0122)$ of Grevesse et al. (2007) is inconsistent with the generally accepted WMAP value $Y_\mathrm{p} = 0.24815$ (Spergel et al. 2007). Nonetheless we adopt $\mathrm{d}Y/\mathrm{d}Z = 2.1$. Table 1 gives the chemical compositions of the isochrones we have employed.

3 STELLAR KINEMATICS

We follow the method of DB98 to calculate the three-dimensional velocity dispersion σ as a function of colour and use a sliding window in $B-V$ with borders that were adjusted to ensure that there are always 500 stars in a window. Every 100 stars a new point is plotted and thus every fifth point is statistically independent of its predecessors. As explained in DB98, the averages we use here are sensitive to outliers, which have to be rejected. We therefore use an iterative method and reject stars that contribute to $\sigma^2 = \sigma_U^2 + \sigma_V^2 + \sigma_W^2$ more than κ^2 times the value of the previous iteration.[1] We use $\kappa = 3.5$ and 6 iterations; 55 stars were rejected.

The red points in Fig. 2 show the resulting run of σ against the mean $B-V$ colour in the sliding windows, with errors in σ shown for every fifth point. Parenago's discontinuity – the abrupt end to the increase in velocity dispersion with $B-V$ (Parenago 1950) – is beautifully visible at $B-V \approx 0.61$. We also calculated σ by combining GCS radial velocities with Hipparcos proper motions, and in Fig. 2 the results are plotted in blue. Where the samples are comparable, there is excellent agreement between the two measurements of σ. At the upper and lower limits of the GCS sample there are discrepancies because the GCS stars were selected by spectral type, so the bluest GCS bins only contain F stars, while the bins from the *Hipparcos* sample contain A and F stars and consequently have a lower mean age. For the reddest bins the situation is the same for G and K stars, but this time counterintuitively the pure G star sample has a higher mean age and velocity dispersion – we explain this phenomenon in Section 5.8.

The diagonal elements of the velocity-dispersion tensor are also of interest, as the stochastic acceleration mechanisms at work are anisotropic so each component of the tensor can evolve independently in time (cf. e.g. GCS). Fig. 3 plots σ_U and σ_V against the mean $B-V$ colour of each bin and Fig. 4 shows σ_W. The three-dimensional dispersion is dominated by the radial dispersion σ_U, which consequently shows the same features as σ. The other two components are different, however, and Parenago's discontinuity is not as beautifully visible in them. For σ_V, the dispersion in the direction of rotation, we notice that the slope changes at $B-V \approx 0.6$, but it continues to increase until $B-V \approx 0.75$. Interestingly, in Fig. 4 the values σ_W from proper motions (red points) show a significant bump at $B-V \approx 0.6$. A similar bump is visible in DB98 but less strikingly so on account of the larger bins used by DB98. Values of σ_W from GCS space velocities have smaller errors and show a less distinctive bump. The GCS error bars on individual components of velocity dispersion are significantly smaller than the corresponding error bars from the larger Hipparcos sample because each Hipparcos star in effect constrains only two components of velocity dispersion. The error bars from the two measurements of σ_W overlap, so the results are not inconsistent. The bump originates from a decrease in average age redwards of the discontinuity that we will explain in Section 5.8. In subsequent work we require a functional fit to the data in Fig. 4. Since the radial velocities add valuable additional information, we fit a 5th-order polynomial to the GCS values where these are available, and elsewhere to the proper-motion values. The black curve in Fig. 4 shows the resulting relation.

As in DB98, the σ_{UV}^2 component of the velocity dispersion tensor is nonzero, implying that the principal axes of σ^2 are not aligned with our coordinate axes. We diagonalised σ^2 to find its eigenvalues σ_i^2, the ratios of the square roots of which are plotted in Fig. 5. The ratio σ_1/σ_2 (red and magenta) shows a slight decrease with increasing $B-V$

---

[1] We use a right-handed coordinate system with x increasing towards the Galactic centre and y increasing in the direction of Galactic rotation.

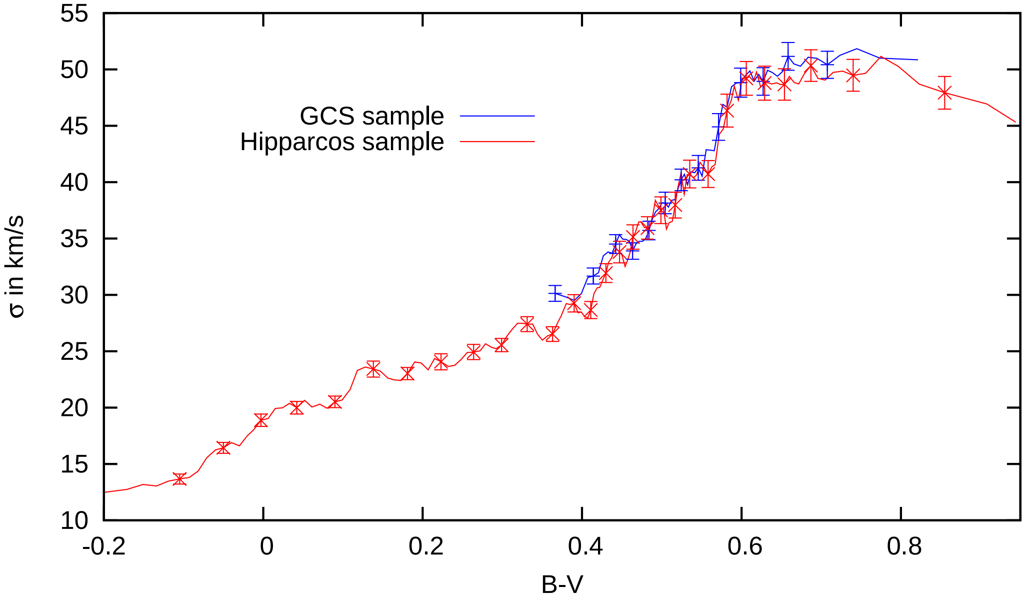

Figure 2. Total velocity dispersion vs. colour. The red line connects the data points for the van Leeuwen–*Hipparcos* proper motions and here and elsewhere only independent data points carry 1σ-errorbars. The blue line is the relation obtained from the GCS space velocities.

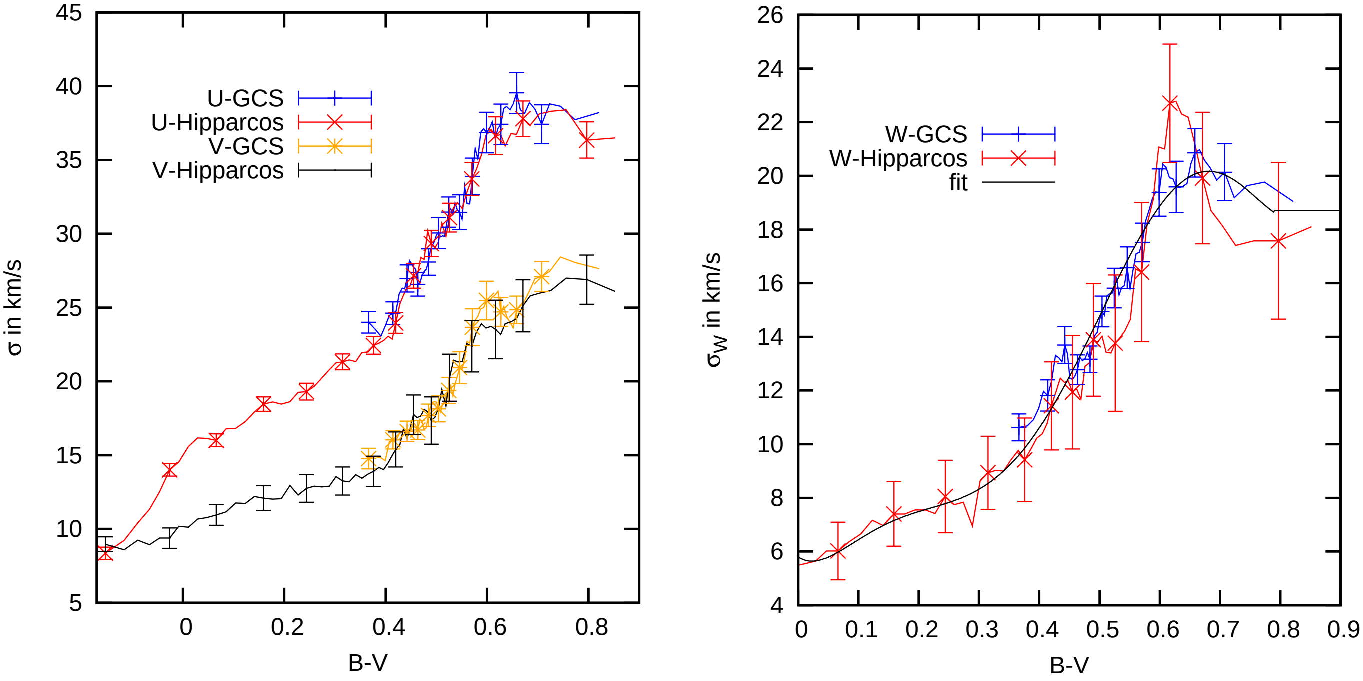

Figure 3. In-plane components of velocity dispersion vs. colour. The red line connects the data points for the σ_U component and the black line connects the data points for the σ_V component, both calculated from the van Leeuwen–*Hipparcos* proper motions with bins of 1000 stars. We also show σ_U and σ_V from the GCS space velocities with bins of 500 stars. Only independent data points carry 1σ-errorbars.

Figure 4. Vertical velocity dispersion vs. colour. The red line connects data points for σ_W from the van Leeuwen–*Hipparcos* proper motions with bins of 1000 stars, while the blue points show values from the GCS space velocities with bins of 500 stars. Only independent data points carry 1σ-errorbars. The black line shows the polynomial fit that is explained in the text and used in subsequent work.

and therefore age, dropping from ~ 1.9 to ~ 1.6 through the range $0.3 < B-V < 0.55$. The ratio σ_1/σ_3 drops from ~ 2.8 for the bluest stars to ~ 2 (judging from the GCS sample) for stars redder than Parenago's discontinuity.

We calculated the sun's velocity with respect to the LSR (U_0, V_0, W_0) as explained in DB98 and found:

$$\begin{aligned} U_0 &= (9.96 \pm 0.33)\,\mathrm{km\,s^{-1}} \\ V_0 &= (5.25 \pm 0.54)\,\mathrm{km\,s^{-1}} \qquad (1) \\ W_0 &= (7.07 \pm 0.34)\,\mathrm{km\,s^{-1}}. \end{aligned}$$

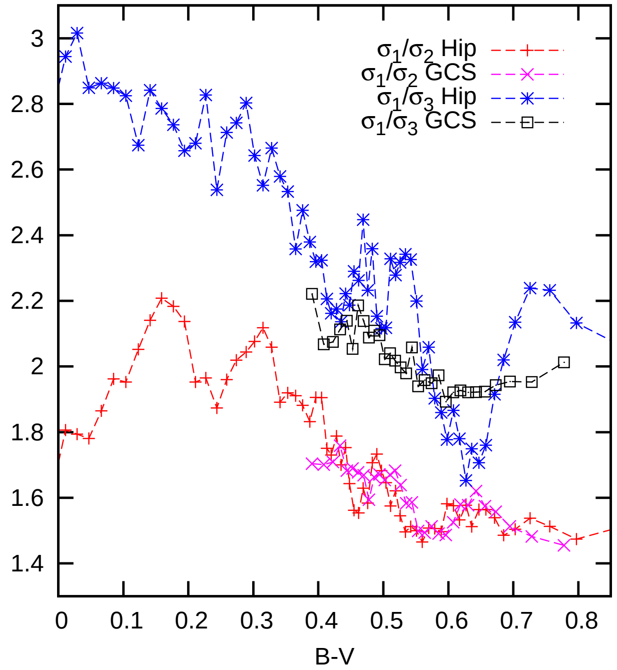

Figure 5. The ratios of the eigenvalues of the velocity dispersion tensor for bins with 1000 stars and a new bin after 200 stars. σ_1/σ_2 from proper motions (red) and GCS space velocities (magenta). σ_1/σ_3 from proper motions (blue) and GCS space velocities (black).

These values are consistent with the results of DB98 but our error bars are smaller by ~ 11 per cent. van Leeuwen (2007), using a sample of $\sim 20\,000$ main-sequence stars selected by imposing only an upper limit for relative parallax errors of 10%, found $U_0 = 10.77 \pm 0.36$, $V_0 = 3.21 \pm 0.52$, in conflict with our values, and $W_0 = 7.04 \pm 0.14$, which is consistent with our findings. Since van Leeuwen's sample extends below the limit to which the *Hipparcos* sample is photometrically complete, his solar motion may be affected by the kinematic biases that are known to be present in the *Hipparcos* input catalogue: stars thought be interesting for a variety of reasons were added to the catalogue, and many such stars had come to the attention of astronomers by virtue of a high proper motion.

Using our values for the solar motion and for σ^2_{xx} to calculate the coefficient in Strömberg's asymmetric drift equation

$$\langle v_y \rangle = -\sigma^2_{xx}/k, \qquad (2)$$

we find $k = 74 \pm 5\,\mathrm{km\,s^{-1}}$, which is lower than, but still consistent with the result of DB98, and also with the estimated scale length of the Galactic disc (Binney & Tremaine 2008, §4.8.2(a)).

As in DB98, we also calculated the vertex deviation l_v, the angle by which one has to rotate the applied Cartesian coordinate system around its $\hat{\mathbf{z}}$ axis to make the velocity dispersion tensor diagonal in the (v_x, v_y) plane. Fig. 6 shows the vertex deviation as a function of colour $B-V$ for bins containing 1000 stars each. As in DB98 the vertex deviation has a minimum at the colour of Parenago's discontinuity. The displayed errors for the Hipparcos sample are slightly larger than in DB98 because we use smaller bins.

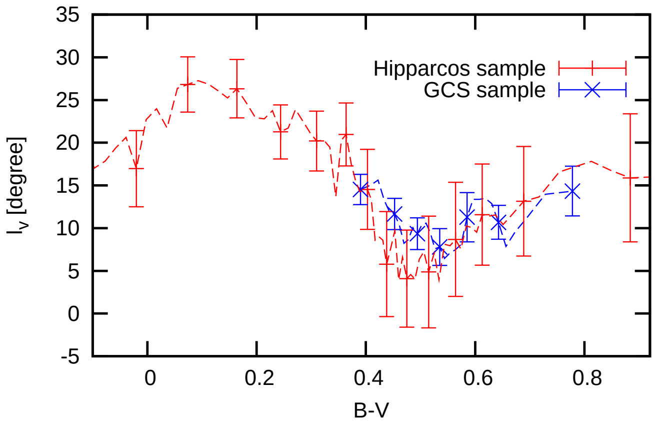

Figure 6. The vertex deviation l_v as a function of colour $B-V$ for bins containing 1000 stars each.

4 MODELLING THE HISTORY OF STAR FORMATION AND HEATING

4.1 Interstellar reddening

For our models, it is important to apply a correction for interstellar reddening to the data because reddening shifts the location of Parenago's discontinuity, which strongly influences the results of our models for the star formation history. BDB00 corrected the data assuming a linear reddening law, $E(B-V) = 0.53\,\mathrm{mag\,kpc^{-1}}$. This law is appropriate for distances of order kiloparsecs, but we live in a low-density bubble within the ISM, so the column density of the ISM and thus the amount of reddening depends on the direction of the line of sight (e.g. Frisch 1995) and for small distances is typically smaller than the mean relation would imply. The code of Hakkila et al. (1997) allows us to determine the reddening as a function of galactic coordinates (l, b), but unfortunately cannot reproduce the results of Lallememt et al. (2003) or Vergely et al. (1998), who find that the reddening within $\sim 70\,\mathrm{pc}$ of the sun is essentially negligible. Recently GCS2 found that reddening is negligible within 40 pc and $E(b-y) = 0.0048$ mag between 40 and 70 pc.[2]

We decided to deredden according to Fig. 4 of Vergely et al. (1998). For stars within 40 pc of the midplane and with a distance from the sun between $d = 70$ and 300 pc, they find $E(b-y) \approx 0.35(d - 70\,\mathrm{pc})/\mathrm{kpc}$, so we have used

$$E(B-V) = \begin{cases} 0 & \text{for } d < 70\,\mathrm{pc} \\ 0.47(d - 70\,\mathrm{pc})/1\,\mathrm{kpc} & \text{otherwise.} \end{cases} \qquad (3)$$

Fig. 7 displays the effect of dereddening on the $(B-V, \sigma)$ diagram by comparing data dereddened according to the old and new prescriptions. The binsize used here was 1000 stars and every 200 stars a new data point was added. We see that BDB00 considerably overestimated the effect of reddening.

---

[2] The conversion factor between colour systems is $E(B-V) \approx 1.35\,E(b-y)$ (Persinger & Castelaz 1990), so GCS2 find $E(B-V) \simeq 0.0065$ between 40 and 70 pc.

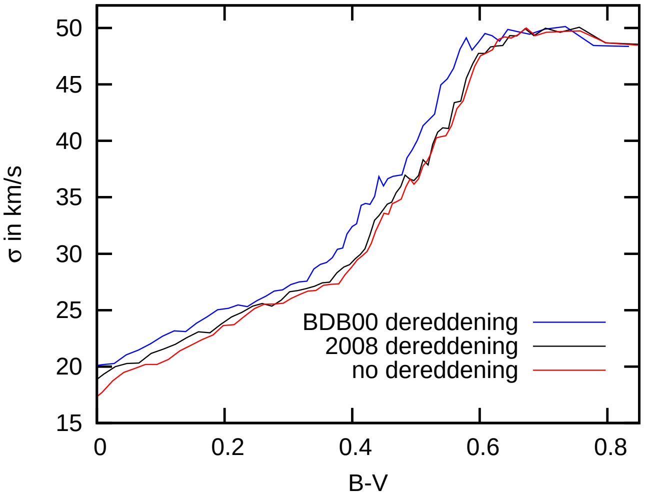

Figure 7. The effect of dereddening on the σ vs. $(B-V)$ diagram for bin sizes of 1000 stars.

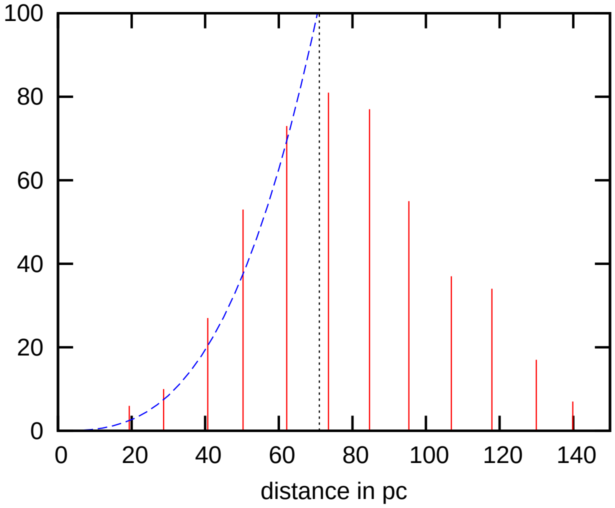

Figure 8. Distance histogram for the colour bin with $0.459 < B-V < 0.476$. The dashed line shows the expected relation for a volume complete sample. The final radius used was 71pc and is indicated by the dotted line.

4.2 Volume completeness

As the velocity dispersion vs. colour $C \equiv B-V$ diagram alone allows models with a rather large variety of parameters, we use the number of stars per colour interval, $\mathrm{d}N/\mathrm{d}C$, as an additional constraint. Our model of the dynamics will predict $N_{\rm cyl}(C)$, the number of stars of a given colour in a vertical cylinder through the disc that has radius $R_{\rm cyl}$ and the sun on its axis. Two points have to be borne in mind when relating this to the observed number density $\mathrm{d}N/\mathrm{d}C$: a) the scale height of stars varies with velocity dispersion and thus colour, and b) the radius of the sphere within which the sample is complete varies with colour.

Assuming the stellar distribution is in equilibrium and neglecting variations with galactic radius, the stellar number density as a function of vertical coordinate z, potential $\Phi(z)$ and vertical velocity dispersion $\sigma_W(C)$ is

$$\nu(z,C) = \nu_0(C)\,\exp\left(-\frac{\Phi(z)}{\sigma_W^2(C)}\right), \qquad (4)$$

where the normalising factor $\nu_0(C)$ is to be determined from the observed density $\mathrm{d}N/\mathrm{d}C$. Integrating $\nu(z,C)$ through the cylinder we have

$$N_{\rm cyl}(C) = \nu_0(C)\pi R_{\rm cyl}^2 \int_{-\infty}^{\infty} \mathrm{d}z\,\exp\left(-\frac{\Phi(z)}{\sigma_W^2(C)}\right). \qquad (5)$$

Integrating $\nu(z,C)$ through the sphere within which the star count is complete at the given colour we have

$$\begin{aligned}\frac{\mathrm{d}N}{\mathrm{d}C} &= \nu_0(C)\pi \int_{-R_c}^{R_c} \mathrm{d}z\,(R_c^2(C)-z^2)\exp\left(-\frac{\Phi(z+z_0)}{\sigma_W^2(C)}\right) \qquad (6)\\ &\equiv \nu_0(C)I(C),\end{aligned}$$

where $R_c(C)$ is the completeness radius and z_0 is the vertical distance of the sun from the galactic midplane. We now have that the normalising constant ν_0 is

$$\nu_0(C) = \frac{\mathrm{d}N/\mathrm{d}C}{I(C)} \qquad (7)$$

and on substituting this into equation (5) we obtain the required relation between $N_{\rm cyl}$ and the star counts $\mathrm{d}N/\mathrm{d}C$. $R_{\rm cyl}$ can be set to any value larger than the largest value of $R_c(C)$. We set $z_0 = 15\,\mathrm{pc}$ (Binney et al. 1997; Joshi 2007) and for $\sigma_W(C)$ we use the polynomial fit shown in Fig. 4. For the potential $\Phi(z)$ we use Model 1 of §2.7 of Binney & Tremaine (2008).

For the determination of R_c we compare the distribution of distances of stars within a radius R in a given colour bin to the distribution we would expect, namely

$$n(R,C) = \nu_0(C)\pi \int_{-R}^{R} \mathrm{d}z\,(R^2-z^2)\exp\left(-\frac{\Phi(z+z_0)}{\sigma_W^2(C)}\right) \qquad (8)$$

The model density $n(R,C)$ depends on R_c through $\nu_0(C)$ and we adjust R_c until we have a value $0.4 < P < 0.6$ for the Kolmogorov–Smirnov (KS) probability that the observed distance distribution at $R < R_c$ is consistent with the model distribution. These comparisons were made for colour bins that contain 500 stars each. Fig. 8 shows a typical histogram and the corresponding model distribution (8). We finally applied a 5th order polynomial fit to the relation $R_c(C)$ (cf. Fig. 9) and used these radii in eqs. (5) and (7) to relate $N_{\rm cyl}$ to $\mathrm{d}N/\mathrm{d}C$. An average of 49 per cent of the stars in a colour bin lie within $R_c(C)$.

A priori, it is not clear, how to choose the exact limits for the KS probability. Fig. 8 might give rise to doubts concerning the completeness out to the chosen value of R_c. However, if we require higher KS probabilities resulting in lower completeness radii and smaller numbers of stars available for analysis, the results do not change in any significant way. We estimated the errors in the number of stars in the column by varying R_c by 10 per cent around our preferred value and by varying σ_W by its 1σ-errors. The resulting error was added in quadrature with the Poisson error. This procedure yielded relative errors that varied from below 10 to 25 per cent, but we imposed a lower limit of 15 per cent on the relative error.

To relate all this to BDB00, Fig. 10 shows our selection function (blue) and that of BDB00 (red). One fundamental difference between BDB00 and this work is that we consider a column stretching to ∞, whereas BDB00 considered a sphere with a radius of $100\,\mathrm{pc}$. In BDB00 stars within this volume more luminous than $5L_\odot$ were assumed to be

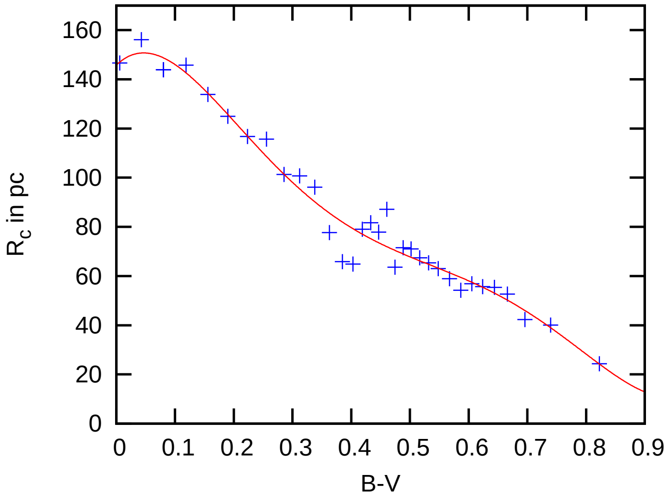

Figure 9. The blue data points show R_c as determined by the Kolmogorov-Smirnov test. The red line displays the applied 5th order polynomial fit.

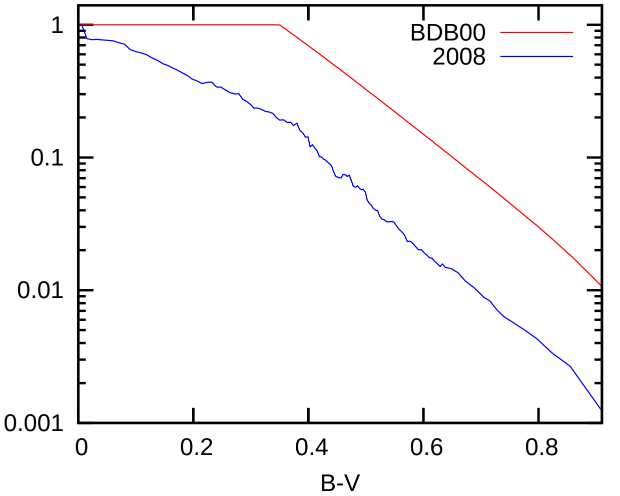

Figure 10. The selection function as in BDB00 (red) and in our models (blue)

complete, and for less luminous stars the radius of completeness was supposed to decrease as $L^{1/2}$. Hence in Fig. 10 the BDB00 selection function is unity bluer than $B-V \sim 0.35$ and then declines linearly. Since we consider a column that extends to infinity, the selection function is always a declining function of luminosity and therefore colour. Hence the most significant difference between the two selection functions is at the blue end where (a) the ability of luminous stars to enter the sample even when far from the plane makes them relatively more numerous in the sample, and (b) the more accurate reduction of the raw *Hipparcos* data by van Leeuwen (2007) has made stars with higher distances available. Even at fainter magnitudes the introduction of the scale-height correction has slightly increased the slope of the selection function, thus depressing the chances of a red star to enter the sample. Consequently, our models have to increase the predicted numbers of red stars in a cylinder relative to the predictions of the BDB00 models.

In summary, roughly half the sample stars contribute to the values of $N_{\rm cyl}$ that we model, but all of the sample stars contribute to the modelled values of the velocity dispersions.

4.3 Distribution over age of stars at a given colour

Following BDB00 the distribution of main-sequence stars in a certain volume over age and mass is given by:

$$\frac{\mathrm{d}^2 N}{\mathrm{d}M\mathrm{d}\tau} \propto \begin{cases} \xi(M)\,\mathrm{SFR}(\tau) & \text{for } \tau < \tau_{\max}(M), \\ 0 & \text{otherwise,} \end{cases} \tag{9}$$

where $\tau_{\max}(M)$ denotes the main-sequence lifetime of a star of initial mass M, $\xi(M)$ the initial mass function and $\mathrm{SFR}(\tau)$ the star formation rate.

BDB00 used a Salpeter-like power-law IMF $\xi(M) \propto M^\alpha$ and an exponential SFR $\propto \exp(\gamma\tau)$. They found that the corresponding characterictic parameters α and γ were strongly correlated (see also Haywood et al. 1997). A high, positive value of γ, i.e. a higher SFR in the past, relatively increases the number of red stars compared to blue stars. This effect can be cancelled by a relatively flat IMF creating more blue stars.

Because of this correlation, we decided to use the IMF of Kroupa et al. (1993):

$$\xi(M) \propto \begin{cases} 1.84\,M^{-1.3} & \text{if } 0.08\,\mathrm{M}_\odot < M < 0.50\,\mathrm{M}_\odot \\ M^{-2.2} & \text{if } 0.50\,\mathrm{M}_\odot < M < 1.00\,\mathrm{M}_\odot \\ M^\alpha & \text{if } 1.00\,\mathrm{M}_\odot < M < \infty. \end{cases} \tag{10}$$

The power-law parameter α for $M > 1.0\,\mathrm{M}_\odot$ has the strongest influence on our results and is thus allowed to vary around $\alpha = -2.7$, the value found by Kroupa et al. (1993).

With the IMF fixed within a small range, we tested several models for the star formation history:

(i) A simple exponential SFR

$$\mathrm{SFR}(\tau) \propto \exp(\gamma\tau) \tag{11}$$

(ii) A SFR of the form

$$\mathrm{SFR}(\tau) \propto A\,\exp(\lambda\tau) + \exp(\gamma\tau), \tag{12}$$

with $\lambda > \gamma$, adding an additional amount of star formation in the early universe.

(iii) A SFR of the form

$$\mathrm{SFR}(\tau) \propto \frac{\tau_2 - \tau}{[(\tau_2 - \tau)^2 + b^2]^2}, \tag{13}$$

as proposed by Just & Jahreiss (2007).

(iv) A smooth SFR overlaid with a factor varying with time according to Fig. 8 of Rocha-Pinto et al. (2000).

We need the isochrones that were described in Section 2.2 to determine the mass range that can be found in a colour interval at a given time. We cut each isochrone off above the point where it is 1.8 mag more luminous than the ZAMS at the same colour. The isochrones provide information only at a limited number of times, so at a desired time one has to interpolate between the next older and next younger isochrones; for the details of this we refer to BDB00.

We can relate $N_{\rm cyl}$ to the average distribution over age in a colour interval (C_-, C_+) by

$$\left\langle \frac{\mathrm{d}N}{\mathrm{d}\tau} \right\rangle_{(C_-,C_+)} = \frac{1}{C_+ - C_-}\frac{\exp(\gamma\tau)}{(1+\alpha)}\sum_j (M_{+,j}^{1+\alpha} - M_{-,j}^{1+\alpha}). \tag{14}$$

Here the sum is over all mass ranges $(M_{-,j}, M_{+,j})$ that lie in the colour interval at age τ.

4.4 Age–metallicity relation

As we use isochrones with a significantly higher number of metallicities than in BDB00, we are able to include a variation of metallicity with age. As guidelines we use the metallicity distribution published in GCS2 and the age–metallicity relation from the models of Schönrich & Binney (2009a, hereafter SB09a), who are able to reproduce the findings of GCS2 and whose results are also consistent with the age–metallicity relation of Haywood (2008).

We find that the GCS2 metallicity distribution has mean $\overline{\mathrm{[Fe/H]}} = -0.12$ and the dispersion 0.17 dex. This result is similar to that of Girardi & Salaris (2001), who found that the metallicity distribution for K giants is well represented by a Gaussian with a mean of -0.12 and a dispersion of 0.18 dex. Haywood (2001) proposed that the distribution was centred on solar metallicity, which shows that the uncertainty is not negligible. Using a Gaussian representation however omits the metal-poor tail of the GCS2 distribution, which comprises approximately 4% of the total sample and spreads in [Fe/H] from -1.2 to -0.4.

From the models of SB09a we extracted that stars with $\mathrm{[Fe/H]} < -0.7$ form only in the first $\sim 0.6\,\mathrm{Gyr}$, stars with $-0.7 < \mathrm{[Fe/H]} < -0.4$ show a high contribution from the time interval $0.5 - 1.5\,\mathrm{Gyr}$, but also a younger component and stars with $\mathrm{[Fe/H]} > -0.4$ started forming after $\sim 0.6\,\mathrm{Gyr}$ and still form today.

We therefore construct a model that features the following two components:

(I) The ‘thin disc’ component

This component comprises $\sim 96\%$ of the model stars and is represented by a Gaussian distribution with the above mentioned mean, so its stars belong to the isochrones with the ten highest metallicities from Table 1. The intrinsic distribution of metallicities will be narrower than the observed one on account of observational errors (cf. Section 5.1). GCS2 conclude that there is no significant change with age in the mean metallicity of solar-neighbourhood stars, so in our models we can consistently use a fit to the current distribution at all times. The models for the star-formation history as described in Section 4.3 and the age $\tau_{\max}$ refer to this component only.

(II) The ‘low-metallicity’ component

For this component we use only the isochrones with the four lowest metallicities from Table 1:

Stars represented by the isochrones with $\mathrm{[Fe/H]} = -0.95$ and -0.78 with contributions of $\sim 0.5\%$ and $\sim 1.0\%$ have ages $\tau \in (\tau_{\max}, \tau_{\max} + 0.6\,\mathrm{Gyr})$.

Stars represented by $\mathrm{[Fe/H]} = -0.65$ with a total contribution of $\sim 1.5\%$; two thirds of these have ages $\tau \in (\tau_{\max} - 0.5\,\mathrm{Gyr}, \tau_{\max} + 0.1\,\mathrm{Gyr})$ and one third has ages $\tau \in (\tau_{\max} - 5\,\mathrm{Gyr}, \tau_{\max} - 0.5\,\mathrm{Gyr})$.

Stars represented by $\mathrm{[Fe/H]} = -0.47$ with a contribution of $\sim 1.0\%$ have ages $\tau \in (\tau_{\max} - 1\,\mathrm{Gyr}, \tau_{\max})$. There is also a significant contribution from stars with this metallicity to the ‘thin disc’ component (cf. Section 5.1).

It would seem desirable to assign a velocity dispersion as high as the one of the ‘thick disc’ to this component, however this significantly diminishes the quality of the fits. We thus model both components with a single disc heating rate as described in the following Section and discuss this result in Section 5.7.

4.5 The disc heating rate

We model the velocity dispersion σ^2 of a group of stars with a known distribution in age by

$$\sigma^2 = \frac{\int_0^{\tau_{\max}} \mathrm{d}\tau\,(\mathrm{d}N/\mathrm{d}\tau)\sigma^2(\tau)}{\int_0^{\tau_{\max}} \mathrm{d}\tau\,(\mathrm{d}N/\mathrm{d}\tau)}. \tag{15}$$

A simple and often used model (e.g. Binney & Tremaine 2008, §8.4), that we will mainly consider here is

$$\sigma(\tau) = v_{10}\left(\frac{\tau + \tau_1}{10\,\mathrm{Gyr} + \tau_1}\right)^{\beta}, \tag{16}$$

where v_{10} and τ_1 characterise the velocity dispersion at 10 Gyr and at birth and β describes the efficiency of stochastic acceleration. However, Quillen & Garnett (2000) argued for saturation of disc heating after $\sim 3\,\mathrm{Gyr}$ and an abrupt increase in velocity dispersion at $\sim 9\,\mathrm{Gyr}$, which they connected to the formation of the thick disc. Therefore we also consider the following model

$$\sigma(\tau) = \begin{cases} v_s\left(\dfrac{\tau + \tau_1}{T_1 + \tau_1}\right)^{\beta} & \text{for} \quad \tau < T_1 \\ v_s & \text{for} \quad T_1 < \tau < T_2 \\ \eta v_s & \text{for} \quad \tau > T_2, \end{cases} \tag{17}$$

where T_1 and T_2 are the times for the occurrence of saturation and the abrupt increase, v_s and ηv_s are the saturation velocity dispersions for the thin and the thick disc and β and τ_1 are as above.

Our velocity dispersion data from Section 3 are not for an infinite cylinder, but for a volume-limited Hipparcos sample. As a coeval population heats, it will spread in z and the fraction of its stars that contribute to the *Hipparcos* sphere will drop. So the contribution of this population to the measured dispersion will be less than that of a younger population. We resolve this problem by introducing a weighting factor $F(\tau) \leqslant 1$ such that a population’s contribution to the measured dispersion is proportional to

$$\left.\frac{\mathrm{d}N}{\mathrm{d}\tau}\right._{\mathrm{heating}} \equiv F(\tau)\left.\frac{\mathrm{d}N}{\mathrm{d}\tau}\right._{\mathrm{cylinder}}. \tag{18}$$

To estimate $F(\tau)$ we consider the conservation of the number of stars born in a certain time interval $\mathrm{d}\tau$ in the approximation that we can neglect radial mixing. Then, as the population heats and spreads in z, its central density drops by a factor $F(\tau)$, which is given by

$$F(\tau)\int_0^{\infty} \mathrm{d}z\,\exp\left(-\frac{\Phi(z)}{\sigma_W^2(\tau)}\right) = \text{constant}. \tag{19}$$

The contribution of a population to any sphere around the sun can now be obtained from equations (5) and (7). For our first fit of the model to the data we take $F(C,\tau) = 1$. The resulting function $\sigma_W(\tau)$ is used to determine $F(C,\tau)$, a new fit is made and F is redetermined. This sequence of operations is rapidly convergent.

The Levenberg–Marquardt non-linear least-squares algorithm (Press et al. 1986) is used to minimise the χ^2 of the fits to the data for $\sigma(B-V)$ and $\mathrm{d}N/\mathrm{d}C(B-V)$. The parameters adjusted are (for the standard disc heating and

SFR model) α, β, γ, $\tau_{\max}$, τ_1 and v_{10}. Data at $B-V<0$ are discarded for fear that the sample of young stars is kinematically biased. As stated above, the stars are binned in sliding windows of 500 stars, a new one every 100 stars. It might seem desirable to use only statistically independent bins (every fifth bin), but then the results turn out to depend on which subset of bins is used. The compromise used was to use every third bin, which reduces the degradation of the information available about the colours at which dispersions change, at the price of yielding values of χ^2 that are slightly too low.

5 THE RESULTS OF THE FITS

As described in BDB00, there are correlations between the parameters which limit the usefulness of the formal errors on the parameters. So we present the results in the following form: we first show the influence of different metallicity weightings on the results and after standardising on a plausible configuration demonstrate the possible range of each parameter by showing the results obtained for fixing it to certain values and leaving the other parameters free. We generally use the total velocity dispersion for our models. The components of σ are studied in Section 5.5.

5.1 The influence of the metallicity weighting

It is interesting to study how our results depend on the weights we assign to the sequence of the ten isochrones in Table 1 with the highest metallicities, which together represent the 'thin disc'. As explained in Section 4.4 we consider three values for the observational scatter in [Fe/H]: 0, 0.1 and 0.12 dex.

GCS2 give the metallicity distribution of F and G dwarfs near the sun, which is a biased measure of the relative numbers of stars formed with each metallicity because stars of a given mass but different metallicities have different lifetimes and luminosities and therefore probabilities of entering a magnitude-limited sample. Fortunately our model simulates this bias; we simply have to choose the weights of the isochrones such that the contribution of each chemical composition to the modelled magnitude-limited sample agrees with the distribution of metallicities in GCS2. Let w_i be the proportion of the SFR which goes into stars of the ith chemical composition. Then the effective weight of this composition is $W_i = F_i w_i / W$, where $W \equiv \sum_i F_i w_i$ and

$$F_i \equiv \int \mathrm{d}(B-V) \int \mathrm{d}\tau \left(\frac{\mathrm{d}N_i}{\mathrm{d}\tau}\right)_{B-V}, \qquad (20)$$

with $(\mathrm{d}N_i/\mathrm{d}\tau)\mathrm{d}\tau$ the number of stars in the given colour and age range that we would have if the whole disc consisted of stars of the ith chemical composition. The w_i are chosen such that after convolution by an appropriate Gaussian distribution of measuring errors the effective weights W_i agree with the metallicity distribution determined by GCS2. The broken curve in Fig. 11 shows the effective weights W_i that correspond to the intrinsic weights w_i of the isochrones, which are shown by the full curve – note that neither curve looks Gaussian because the bins have varying widths. We see that the effective weights are biased towards low metallicities relative to the intrinsic weights w_i.

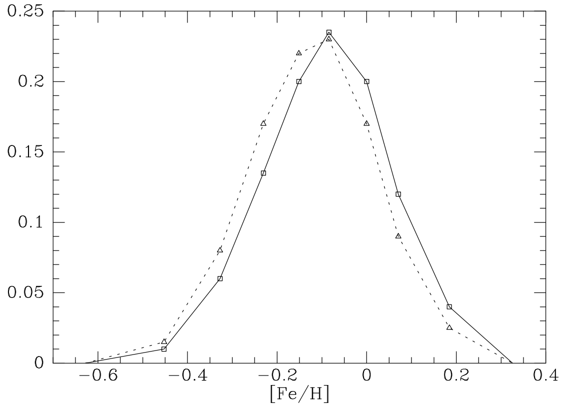

Figure 11. The full curve joins the intrinsic weights w_i of the isochrones $i=3,\ldots,12$ for the 'thin disc' component that yield the effective weights W_i of the isochrones in a magnitude-limited sample like that of GCS2 that are joined by the dashed curve. After convolution by a Gaussian distribution of observational errors with dispersion $\Delta_{[\mathrm{Fe/H}]} = 0.1$ dex the W_i are consistent with the metallicity distribution of GCS2.

The adopted metallicity distribution of the 'thin disc' component hardly affects the results of the best fit. All parameters and the fit quality are very stable, as is shown in Table 2. As the construction of the low-metallicity component is not straight-forward, we also tested models without this component. The results are also presented in Table 2. For those models the age $\tau_{\max}$ depends strongly on the metallicity distribution in the sense that the stronger the low-metallicity tail of the distribution, the larger is the recovered value of $\tau_{\max}$. Consequently, $\tau_{\max}$ decreases as we increase our estimate of the errors Δ_{FeH} in the GCS metallicities because the larger the measurement errors, the narrower the distribution of intrinsic metallicities used in the model. The models without a low-Z component generally show better fit qualities than the two-component models, but broadly speaking all fits are in the same quality range. The old, low-metallicity component is constrained to a relatively small colour interval, whereas for the one-component model, the low-metallicity stars cover all ages and thus a wider colour interval, resulting in a better fit quality. All models with a significant low-metallicity component show very similar ages $\tau_{\max} \sim 12.5$Gyr.

All the ages in Table 2 are larger than the value 11.2 ± 0.75 Gyr obtained by BDB00, principally because the reduction in the estimate of reddening shifts Parenago's discontinuity to the red, where the average age of stars is higher. The age could be brought down by lowering the helium abundance of the low-Z isochrones, which would shift the isochrones to redder colours. However, values of Y significantly below the value of Y_{p} from WMAP would be required to reduce $\tau_{\max}$ appreciably. Interestingly, Casagrande et al. (2007) found very low Helium abundances for nearby K-dwarfs using Padova isochrones.

For the following sections we decided to use two-component models with a 'thin-disc' metallicity distribution corresponding to measurement errors of $\Delta_{\mathrm{FeH}} = 0.1$ dex and an intrinsic dispersion of 0.14 dex.

Table 2. The parameters for the best fits to the data at different metallicity distributions and the fit quality χ^2. The metallicity distribution of the 'thin disc' component is characterised by the effective weights of the isochrones with the ten highest values of [Fe/H] in Table 1

$\Delta_{\rm [Fe/h]}$ dex	effective weights W_i 'thin disc' comp. low → high Z in %	α	β	γ Gyr^{-1}	$\tau_{\rm max}$ Gyr	τ_1 Gyr	v_{10} km s^{-1}	χ^2
	with low met. tail							
0	(0.4, 3.5, 10.0, 16.0, 18.5, 19.5, 16.0, 11.0, 4.4, 0.7)	−2.559	0.356	0.117	12.557	0.187	55.187	1.05
0.1	(0.0, 1.5, 8.0, 17.0, 22.0, 23.0, 17.0, 9.0, 2.5, 0.0)	−2.549	0.349	0.117	12.602	0.149	55.179	1.04
0.12	(0.0, 0.7, 6.0, 17.0, 24.0, 26.0, 17.5, 7.5, 1.3, 0.0)	−2.571	0.350	0.115	12.601	0.148	55.232	1.06
	without low met. tail							
0	(0.4, 3.5, 10.0, 16.0, 18.5, 19.5, 16.0, 11.0, 4.4, 0.7)	−2.519	0.385	0.119	12.606	0.261	57.157	0.92
0.1	(0.0, 1.5, 8.0, 17.0, 22.0, 23.0, 17.0, 9.0, 2.5, 0.0)	−2.673	0.375	0.121	11.980	0.201	57.588	0.94
0.12	(0.0, 0.7, 6.0, 17.0, 24.0, 26.0, 17.5, 7.5, 1.3, 0.0)	−2.610	0.376	0.130	11.782	0.190	57.975	1.03

Table 3. The effect of varying β on the fits. For α and $\tau_{\rm max}$ upper limits of −2.400 and 13.000 Gyr were set.

α	β fixed	γ Gyr^{-1}	$\tau_{\rm max}$ Gyr	τ_1 Gyr	v_{10} km s^{-1}	χ^2
−2.400	0.250	0.141	13.000	0.001	48.257	3.78
−2.445	0.300	0.119	13.000	0.001	52.615	1.29
−2.549	0.349	0.117	12.602	0.149	55.179	1.04
−2.643	0.420	0.112	12.281	0.486	57.449	1.19
−2.722	0.500	0.120	11.605	0.978	58.963	1.58

5.2 Varying β

Table 3 shows the results of fixing β, the exponent in the heating rate, and Fig. 12 shows the fits obtained with the best value ($\beta = 0.349$) and fits for values of β that are just too large ($\beta = 0.500$) and clearly too small ($\beta = 0.250$) to be acceptable. For $\beta = 0.250$ the dependence of σ on $B-V$ is too flat and we obtain a poor fit to the number counts. Judging from the results, we are able to exclude values of $\beta \lesssim 0.28$. The fit for $\beta = 0.500$ is relatively bad for the N-data of red stars and the corresponding $\sigma(B-V)$ is too flat for blue stars and too steep just before and around Parenago's discontinuity. In view also of the large χ^2, and the high velocity dispersion at birth (17.6 km s^{-1}), we conclude that $\beta \geqslant 0.50$ can be excluded.

When β is increased, the program increases v_{10} and τ_1 in an effort to keep the general shape of $\sigma(\tau)$ constant. Since the velocity dispersion of red stars strongly constrains $v_{10}\tau_{\rm max}^{\beta}$, the increase in v_{10} is compensated by a decrease in $\tau_{\rm max}$. As the isochrones have limted age ranges, we generally set an upper limit for $\tau_{\rm max}$ at 13.0 Gyr. α and γ are relatively stable for the different values of β. α is only allowed to vary around the Kroupa et al. (1993) value −2.7 within the interval (−2.4, −3.0).

5.3 Varying the age

We now examine the effect of optimising the other parameters for fixed age $\tau_{\rm max}$. The favoured ages are higher than in BDB00 and surprisingly large in relation to the accepted age of the universe $\tau_{\rm H} = 13.7$ Gyr. So we fixed $\tau_{\rm max}$ at values $\geqslant 9$ Gyr to see if acceptable younger models could be found. Table 4 shows the results and Fig. 13 displays three fits to the data.

Table 4. The effect of varying $\tau_{\rm max}$ on the fits. For the lowest ages considered, α was fixed at −2.400.

α	β	γ Gyr^{-1}	$\tau_{\rm max}$ fixed	τ_1 Gyr	v_{10} km s^{-1}	χ^2
−2.510	0.338	0.112	13.000	0.103	54.758	1.07
−2.549	0.349	0.117	12.602	0.149	55.179	1.04
−2.503	0.357	0.131	12.000	0.182	55.495	1.07
−2.470	0.363	0.153	11.500	0.215	55.499	1.18
−2.400	0.375	0.173	11.000	0.276	55.696	1.30
−2.400	0.383	0.195	10.500	0.307	55.951	1.43
−2.400	0.393	0.217	10.000	0.361	56.124	1.72
−2.400	0.404	0.274	9.000	0.394	56.594	2.55

γ increases with decreasing age as the ratio of old stars to young stars is an important constraint influencing both $\sigma(B-V)$ and $\mathrm{d}N/\mathrm{d}C$. α slightly increases with increasing γ, but is relatively stable. As explained above, low ages are associated with higher values of β, τ_1 and v_{10}.

Judging from the values of χ^2 listed in Table 4, ages above 11.5 Gyr are certainly accepted and ages of 10 Gyr and lower can be excluded. From Fig. 13 we see that the problem with low ages lies in the reddest bins, in both the N and the σ data. The fit for 9 Gyr is definitely unable to represent the data and such low ages have to be excluded. For 10.5 Gyr, χ^2 is still reasonable but the fit redwards of $B-V = 0.55$ looks bad. In view of the development of χ^2 for ages between 11.5 and 10 Gyr, we can set a conservative lower age limit ~ 10.5 Gyr.

5.4 The velocity dispersion at birth and after $\tau_{\rm max}$

The correlations of the parameters τ_1 and v_{10}, which determine the velocity dispersion at birth and for the oldest stars, have already been discussed. v_{10} only varies within a narrow range, as it is strongly constrained by the observed velocity dispersion redwards of Parenago's discontinuity. As Table 5 shows, the data allow a wide range of τ_1 values that correspond to velocity dispersions at birth between 0 and ~ 15 km s^{-1}. The effect of this parameter is quite small as

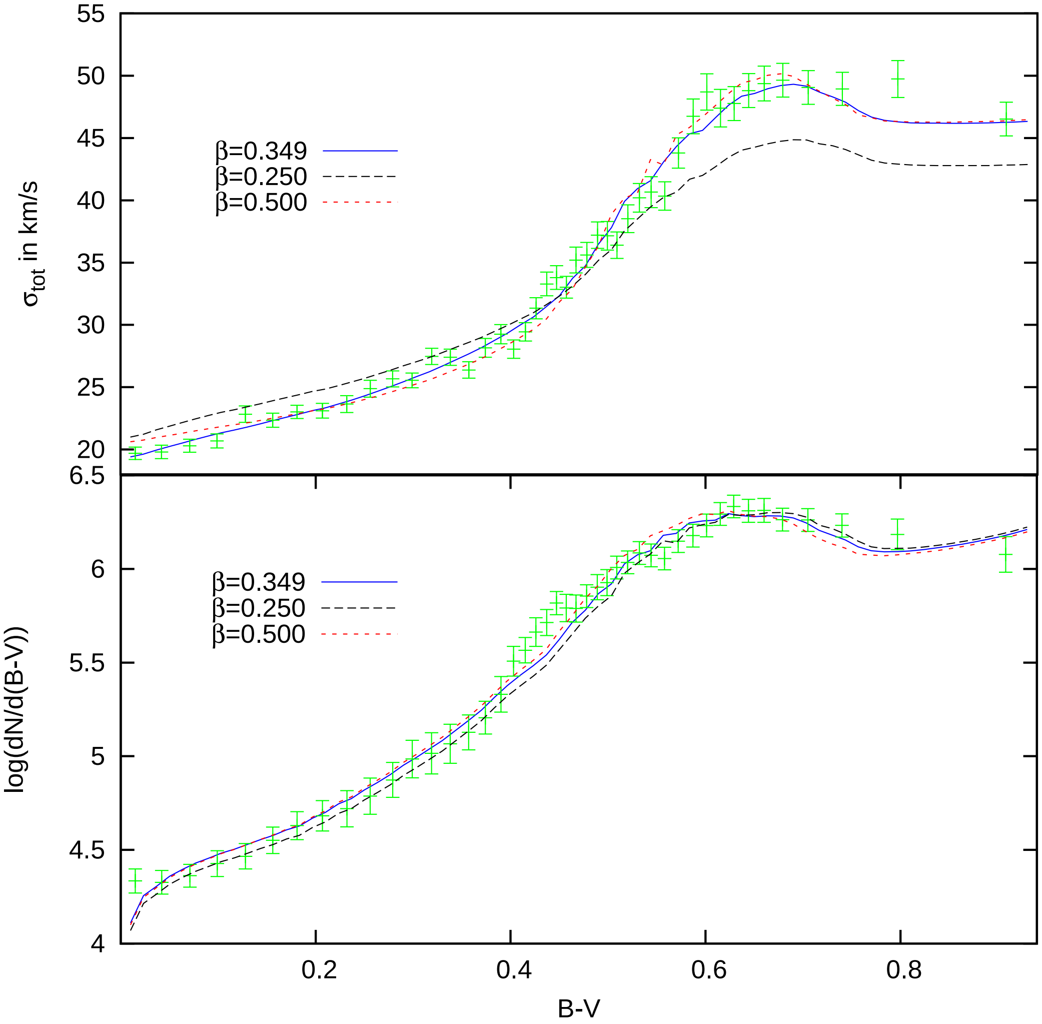

Figure 12. Fits to the data for different values of β. *Upper panel:* Total velocity dispersion, *Lower panel:* Projected number in the solar cylinder per colour bin. *Green*: Input Data, *Long dashed, black*: $\beta = 0.250$, *Blue*: $\beta = 0.349$, *Short dashed, red*: $\beta = 0.500$.

Table 5. The effect of varying the parameter characterising the velocity dispersion at birth τ_1 on the fits.

σ_{birth} $\mathrm{km\,s^{-1}}$	σ_{final} $\mathrm{km\,s^{-1}}$	α	β	γ $\mathrm{Gyr^{-1}}$	$\tau_{\max}$ Gyr	τ_1 fixed	v_{10} $\mathrm{km\,s^{-1}}$	χ^2
0.00	58.90	−2.400	0.317	0.117	13.000	0.000	54.200	1.11
8.14	59.46	−2.519	0.329	0.116	12.673	0.030	55.056	1.09
12.65	61.82	−2.549	0.349	0.117	12.602	0.149	55.179	1.04
16.04	61.36	−2.635	0.416	0.119	12.096	0.500	56.944	1.17
17.27	62.22	−2.728	0.462	0.119	12.020	0.800	57.483	1.39

the power-law leads to a steep increase of velocity-dispersion within a time small compared to $\tau_{\max}$. As the dispersion is already $20\,\mathrm{km\,s^{-1}}$ for the bluest bin, the adjustment of the parameters to fit $\sigma(B-V)$ is a minor issue.

5.5 Studying the components of σ

As the results in Section 3 have shown, the three components of σ show significantly different behaviours: their ratios vary with colour and Parenago's discontinuity is sharper in some components than in others. Therefore we now seek separate models for the evolution of each eigenvalue of σ^2. Since all three models have to satisfy the same N data, and the errors on the eigenvalues of σ^2 are larger than those on σ_{total}, we fix the parameters that describe the star formation history at the best-fit values determined above for σ_{total}, namely $\alpha = -2.55$, $\gamma = 0.117$ and $\tau_{\max} = 12.5\,\mathrm{Gyr}$, and determined for each eigenvalue of σ^2 only values of the heating parameters, β, τ_1 and v_{10}. The data for σ_W were represented by the polynomial fit shown in Fig. 4.

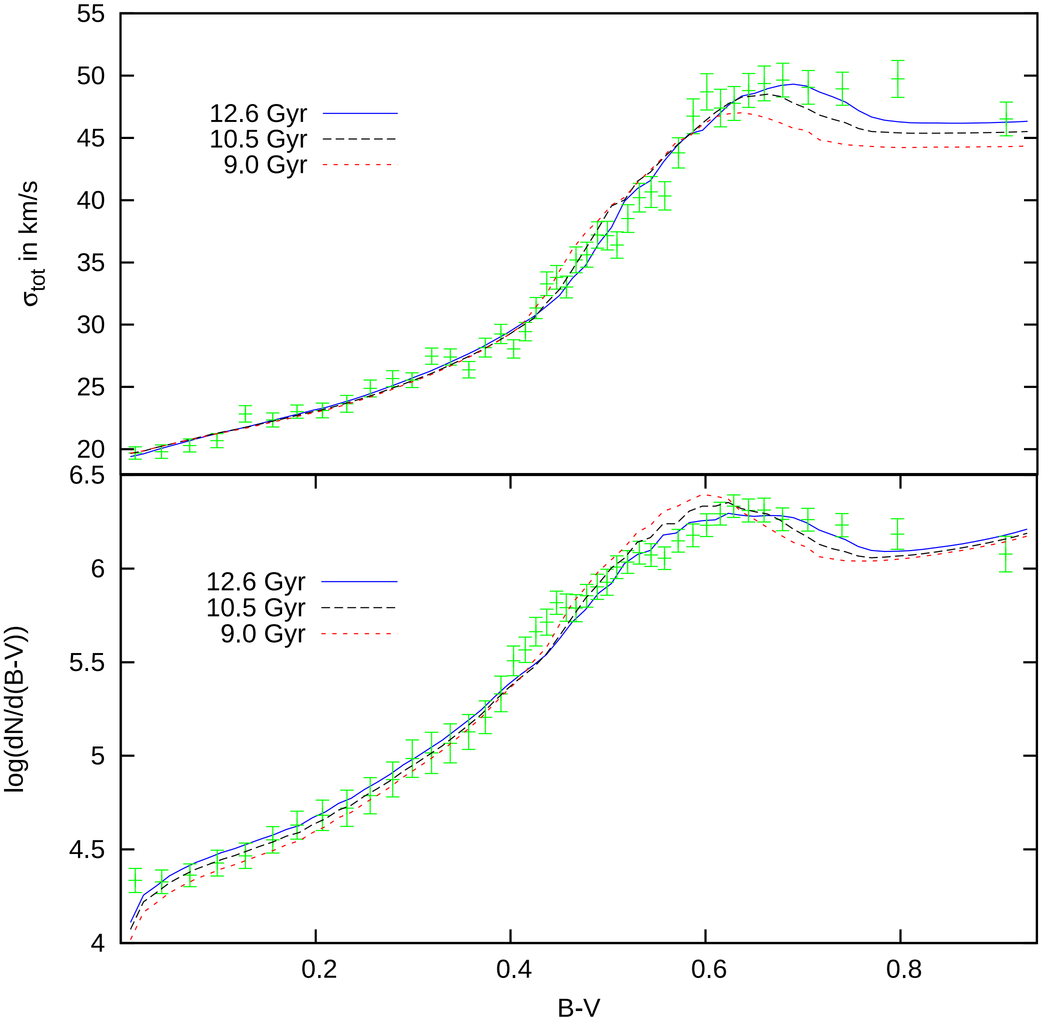

Figure 13. Fits to the data for different values of $\tau_{\max}$. *Upper panel:* Total velocity dispersion, *Lower panel:* Projected number in the solar cylinder per colour bin. *Green*: Input Data, *Blue*: $\tau_{\max} = 12.6$Gyr, *Long dashed, black*: $\tau_{\max} = 10.5$Gyr, *Short dashed, red*: $\tau_{\max} = 9.0$ Gyr.

Table 6. Fits to the data for the three different components of σ.

	β	τ_1 Gyr	v_{10} km s^{-1}	χ^2
σ_U	0.307	0.001	41.899	0.83
σ_V	0.430	0.715	28.823	0.51
σ_W	0.445	0.001	23.831	0.43

Table 6 shows the best-fit values of the parameter and χ^2. The latter are quite small for σ_V and σ_W because the formal errors on these components are large. Compared to $\beta_{\rm total}$, $\beta_U = 0.307$ is lower, so the heating exponents for the other two components are higher than 0.349. Consequently, $\beta_V = 0.430$ and $\beta_W = 0.445$ are significantly larger than β_U.

The three β values are consistent with Figure 5 in the sense that σ_1/σ_2 and σ_1/σ_3 both decrease with increasing $B-V$ and thus increasing mean age, and σ_1/σ_3 decreases more steeply than σ_1/σ_2, indicating that $\beta_W > \beta_V > \beta_U$, which is what we find. However, it has to be mentioned, that because of the rather large interval of acceptable values for β encountered in Section 5.2, we cannot exclude $\beta_W \leqslant \beta_V$.

Table 7. The effect of varying γ at fixed $\alpha = -2.7$ on the fits. As an upper limit for the age $\tau_{\max}$ we apply 13.0 Gyr.

α fixed	β	γ fixed	$\tau_{\max}$ Gyr	τ_1 Gyr	v_{10} km s^{-1}	χ^2
−2.700	0.347	0.140	12.044	0.147	54.898	1.21
−2.700	0.349	0.120	12.542	0.144	55.237	1.07
−2.700	0.348	0.100	13.000	0.136	55.396	1.06
−2.700	0.359	0.080	13.000	0.163	56.280	1.12
−2.700	0.371	0.060	13.000	0.194	57.195	1.47

5.6 Different approaches to the SFR

α and γ are strongly correlated. A high, positive value of γ, i.e. a higher SFR in the past, increases the number of red stars relative to blue stars. This effect can be cancelled by a

Table 8. The results for a SFR with two timescales. The two input parameters are displayed on the left, the output as usual on the right, followed by the characteristic model parameters ϑ and ρ. Keep in mind the best χ^2 for the chosen metallicity distribution was 1.04.

A	λ Gyr^{-1}	α	β	γ Gyr^{-1}	$\tau_{\max}$ Gyr	τ_1 Gyr	v_s km s^{-1}	ϑ	ρ	χ^2
3×10^{-12}	3.0	−2.512	0.346	0.095	10.022	0.132	54.968	13.2	0.21	1.19
1×10^{-12}	3.0	−2.530	0.346	0.092	10.363	0.137	54.979	13.2	0.18	1.10
3×10^{-13}	3.0	−2.527	0.345	0.098	10.741	0.145	54.823	10.3	0.15	1.10
3×10^{-8}	2.0	−2.538	0.349	0.085	10.233	0.147	55.145	9.7	0.21	1.18
1×10^{-8}	2.0	−2.501	0.348	0.093	10.727	0.162	54.821	7.7	0.16	1.11
3×10^{-9}	2.0	−2.530	0.349	0.089	11.333	0.170	54.780	7.6	0.14	1.10
3×10^{-4}	1.0	−2.527	0.350	0.073	10.604	0.170	55.058	5.6	0.22	1.18
1×10^{-4}	1.0	−2.530	0.345	0.092	11.416	0.159	54.574	3.2	0.14	1.12

relatively flat IMF creating more blue stars. For the investigation of different star formation histories, we thus fixed α at the Kroupa et al. (1993) value of -2.7 and tested different values of γ. The best fit in Section 5.3 showed a less steep IMF, so we expect now to find that the model with lowest χ^2 has a lower value of γ. Table 7 confirms that this is the case. In all the above Sections, the SFR is decreasing: for the best fit from Section 5.3, it decreases by a factor 4.4 between the beginning of star formation until now. Combining Tables 7 and 4, factors between 2.2 and 6.7 are plausible.

For values of $\gamma \leqslant 0.1$, we had to fix the age $\tau_{\max}$ to 13.0 Gyr for the reason given above. Our models generally need a large number of old stars. Since stars 10 Gyr and older move very slowly in the CMD, it is interesting to ask whether acceptable models with a reduced lower age limit can be obtained by permitting a high SFR early on. Moreover, a short early period of intense star formation is envisaged in the popular proposal that the thick disc formed as a result of a major accretion event ~ 10 Gyr ago (e.g. Chiappini et al. 2001).

We thus applied a SFR as described by equation (12). The timescale of the first formation epoch should be small compared to $\tau_{\max}$, so we tried $\lambda = 1$, 2 and 3 Gyr^{-1}. The results for different parameters A are displayed in Table 8.

The fraction ρ of solar-neighbourhood stars that belong to the 'thick disc' is determined by A and λ. Table 8 gives ρ for each model – observationally Juric et al. (2008) found $\rho \approx 0.11$ for their definition of the thick disc, so we used this value as a guidance in adjusting the parameters. We further characterise the scenarios by the ratio of the two terms at the beginning of star formation: $\vartheta = A \exp[(\lambda - \gamma)\tau_{\max}]$. Since models with very small A are indistinguishable from standard pure-exponential models, we stopped lowering A when χ^2 reached a value comparable to that of the best-fitting standard model. Significantly, no two-exponential model achieved a lower χ^2 than the best standard model.

For all scenarios, the parameters α, β, τ_1 and v_{10} are very stable; the disc-heating parameters do not depend significantly on the applied SFR, so there is no need for a further discussion. Compared to its values from Section 5.3, γ has decreased for the lower ages to compensate for the influence of the added 'thick disc' SFR term. The most striking difference is that the favoured ages have decreased by ~ 1.0 Gyr. The best results were achieved for $\lambda \geqslant 2.0$ Gyr^{-1}. For the SFR considered here, the lower age limit has to be lowered to ~ 10.0 Gyr.

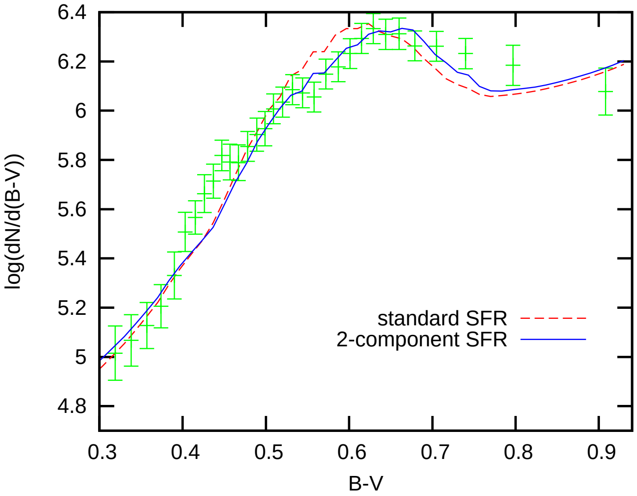

Figure 14. The fits to the N-data for a standard SFR 10.5 Gyr model and a two-component ($\lambda = 2.0$, $A = 10^{-8}$) 10.7 Gyr model in the relevant $B - V$ interval.

Fig. 14 compares the fits to the N data for the 10.5 Gyr model of Section 5.3 and the 10.7 Gyr model with $\lambda = 2$ Gyr^{-1} and $A = 10^{-8}$. It shows how the intense first period of star formation improves the fits to the data of the red colour bins at lower disc ages.

Rocha-Pinto et al. (2000) argue that the SFR of the solar neighbourhood is very irregular. They also find that the SFR shows an increasing tendency, which is incompatible with our findings. It is however interesting to ask if it is possible to achieve reasonable fits with a smooth SFR overlaid with factor varying in time according to Fig. 8 of Rocha-Pinto et al. (2000). The best fit for this approach has a χ^2 of 1.44 and is characterised by the following parameters

$$\alpha = -2.635 \quad \beta = 0.354 \quad \gamma = 0.120$$
$$\tau_{\max} = 12.266 \quad \tau_1 = 0.159 \quad v_{10} = 56.488,$$

which are all in the range of acceptable values as determined above. The higher value of χ^2 results from additional features, which are produced by the varying SFR and which are incompatible with the data. We are, however, not able to exclude a SFR which is not smooth. As Figures 12 and 13

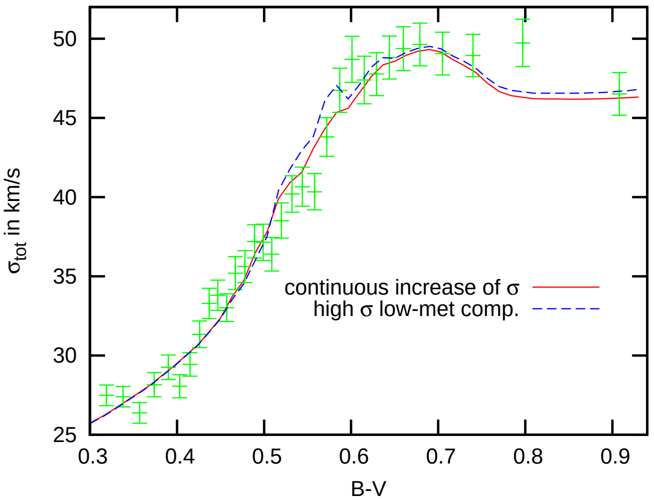

Figure 15. The effect of assigning a high velocity dispersion $\sigma_{tot} = 85\,\mathrm{km\,s^{-1}}$ to the low-metallicity component.The red line shows the best fit from above.

show, there are features in the data that our models are not able to reproduce and which might be produced by epochs of enhanced star formation.

We finally test the SFR described by equation (13), which was proposed by Just & Jahreiss (2007). This SFR increases early on and then decreases. The best-fit model achieves $\chi^2 = 1.15$ with

$$\begin{aligned} &\tau_2 \approx 14\,\mathrm{Gyr} \\ &\alpha = -2.400 \qquad \beta = 0.334 \qquad b = 7.230 \\ &\tau_{\max} = 12.686 \qquad \tau_1 = 0.094 \qquad v_{10} = 54.392. \end{aligned}$$

In this model the SFR peaked $\sim 10.3\,\mathrm{Gyr}$ ago and has since decreased by a factor ~ 4. The fit provided by this is of a similar quality as the best fits with the standard SFR, and the values of all comparable parameters are little changed from when we used the standard SFR.

5.7 Different Approaches to the heating rate

In our models we have so far assumed that the velocity dispersion increases continuously with age. In the context of the Galactic thick disc, an obvious question to ask is what would be the effect of assigning a high velocity dispersion, $\sigma_{\rm tot} = 85\,\mathrm{km\,s^{-1}}$ (Bensby et al. 2004), to the low-metallicity component. Fig. 15 shows that this procedure produces an additional feature in the curve $\sigma_{\rm tot}(B-V)$ that underlines again the narrow colour interval to which the low-metallicity component is confined. The reason for this is that the thick disk is not only metal-poor and old, but has a more complex structure (Schönrich & Binney 2009b).

In this context it is also interesting to study whether a saturation of disc heating, or a merger event producing a discontinuity in the time evolution of σ, or a combination of the two is compatible with the data. We adopt the alternative model (17) of $\sigma(\tau)$. This model introduces three additional parameters, T_1 when heating saturates, T_2 when there is a step increase in σ and η, the scale of that increase.

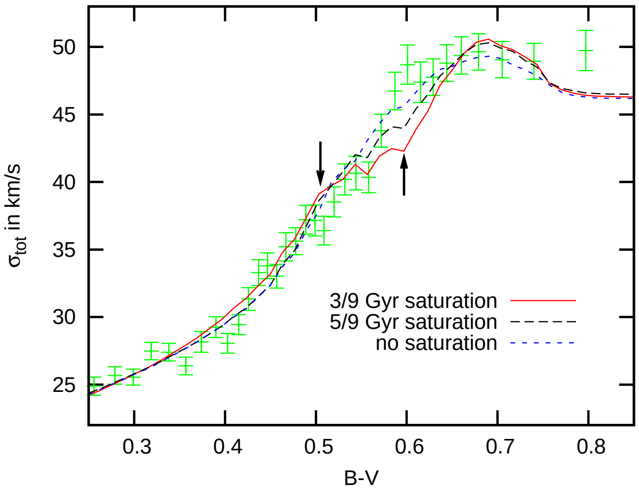

Figure 16. The fits for two different saturation scenarios with $(T_1,\ T_2,\ \eta) = (3\,\mathrm{Gyr},\ 9\,\mathrm{Gyr},\ 1.5)$ (red) and $(5\,\mathrm{Gyr},\ 9\,\mathrm{Gyr},\ 1.5)$ (black, long dashed). The blue, short dashed curve is the best fit without saturation. The black arrows indicate the two additional discontinuities in the 3/9 Gyr scenario.

Table 9 provides an overview of results obtained by fixing these parameters.

We start by looking at a pure saturation of disc heating ($\eta = 1$) with $T_1 = 5$, 6 and 7 Gyr. Intuitively, this model is incompatible with the phenomenon of Parenago's discontinuity unless $T_1 \gtrsim 7\,\mathrm{Gyr}$, and that is what the results confirm. For $\eta = 1$ we can firmly exclude $T_1 \leqslant 5\,\mathrm{Gyr}$.

Consider now the proposal of Quillen & Garnett (2000) that $T_1 = 3\,\mathrm{Gyr}$, $T_2 = 9\,\mathrm{Gyr}$ and $\eta \gtrsim 1.5$. Our best fit, obtained with $\eta = 1.75$, is shown by the red curve in Fig. 16. The curve of $\sigma(B-V)$ moves from the high to the low side of the data around $B-V = 0.55$ as a result of two changes in slope at the points marked by arrows; at these points the main-sequence age corresponds to T_1 and T_2. This figure and the high χ^2 given in Table 9 exclude this model.

To see whether the unwanted features associated with T_1 and T_2 could be washed out by an irregular star-formation history rather than the smooth one used in our models, we modelled the data using $T_1 = 3\,\mathrm{Gyr}$, $T_2 = 9\,\mathrm{Gyr}$, $\eta = 1.75$ and overlaying our smooth SFR with a factor varying with time according to Fig. 8 of Rocha-Pinto et al. (2000). The resulting fit to the data, shown by the long-dashed line in Fig. 17, is even worse than that shown in Fig. 16. Another possibility is that large errors in $B-V$ ($\sim 0.023\,\mathrm{mag}$) could smooth away the unwanted discontinuities. To test this hypothesis we folded $\sigma(B-V)$ for the $(3\,\mathrm{Gyr},\ 9\,\mathrm{Gyr},\ 1.75)$ model with a Gaussian of 0.023 mag dispersion. Still the discontinuities did not disappear (short-dashed curve in Fig. 17).

Acceptable models can be found by allowing T_1 to approach T_2 with corresponding adjustment to η. For example, the fit provided by the $(5\,\mathrm{Gyr},\ 9\,\mathrm{Gyr},\ 1.5)$ model is shown as the black curve in Fig. 16: the fit to $\sigma(B-V)$ is clearly better than that for $(3\,\mathrm{Gyr}, 9\,\mathrm{Gyr}, 1.75)$ model and nearly as good as the best fit without saturation (blue curve). Overall one has the impression that models with T_1 close to T_2 are merely approximating a power-law dependence with an appropriate step.

Table 9. The results for the assumption of a saturation of disc heating. The three input parameters are displayed on the left, the output as usual on the right. Keep in mind the best χ^2 for the chosen metallicity distribution was 1.04. An upper age limit was set at 13.0 Gyr.

T_1 Gyr	T_2 Gyr	η	α	β	γ Gyr^{-1}	$\tau_{\max}$ Gyr	τ_1 Gyr	v_s $\mathrm{km\,s}^{-1}$	χ^2
5.0	–	1.0	−2.493	0.588	0.114	13.000	0.845	49.468	1.69
6.0	–	1.0	−2.413	0.477	0.117	13.000	0.558	50.245	1.37
7.0	–	1.0	−2.480	0.429	0.119	12.556	0.396	52.044	1.17
3.0	9.0	1.50	−2.564	1.986	0.126	12.539	5.801	41.004	1.51
3.0	9.0	1.75	−2.509	0.484	0.132	12.003	0.488	38.483	1.45
3.0	9.0	2.00	−2.509	0.458	0.151	11.708	0.489	37.213	1.67
3.0	8.0	1.50	−2.448	0.606	0.127	12.017	0.915	38.929	1.37
4.0	9.0	1.60	−2.457	0.367	0.131	12.043	0.205	40.606	1.22
5.0	9.0	1.50	−2.495	0.334	0.132	12.046	0.127	42.646	1.12

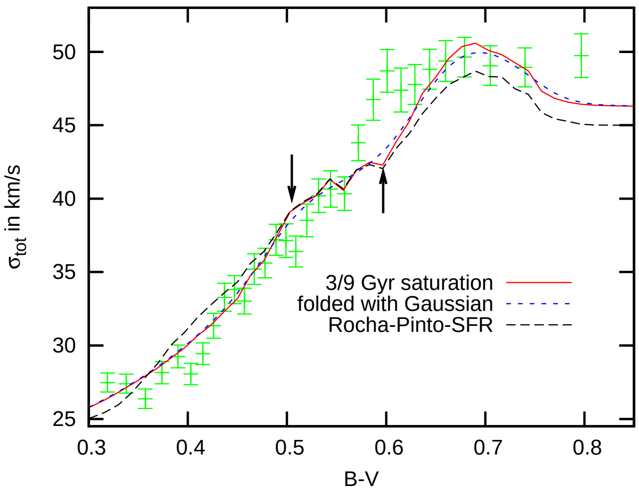

Figure 17. Attempts to smooth out the discontinuities in the (3 Gyr, 9 Gyr, 1.75) σ-plot (red curve). A) Smooth SFR overlaid with a variation in time according to Rocha-Pinto et al. (2000) (black, long dashed). B) Folded with a Gaussian with a dispersion equivalent to the error in colour $B-V$ (blue, short dashed)

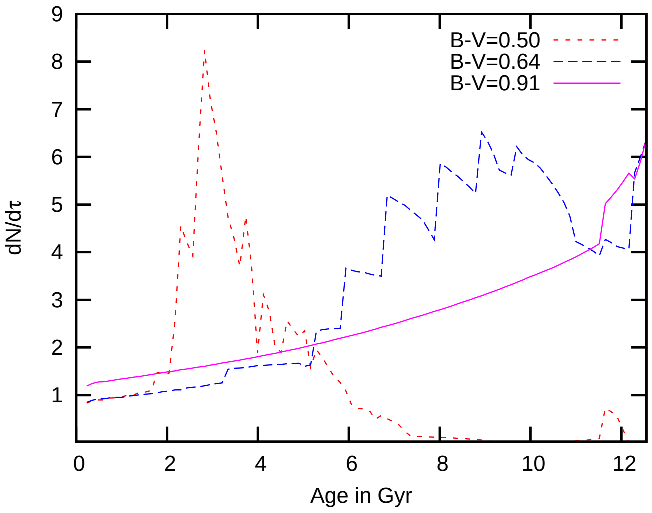

Figure 18. The age distribution of the 12.6 Gyr fit from Section 5.3 for three mean colours.

5.8 Why does σ decrease redwards of the discontinuity?

All plots of $\sigma(B-V)$, whether for models or data, show a counterintuitive decrease in sigma for the reddest bins: the velocity dispersion in our models increases with age, so decreasing σ implies a decrease in mean age as one moves redwards of the discontinuity. Fig. 18 shows model age distributions at $B-V \approx 0.50$, 0.65 and 0.90. For the reddest colour we see only a smooth increase in numbers with age, reflecting the declining SFR, and a feature at high ages, resulting from the low-metallicty component. At the bluer colours we have strong features. From equation (14) we see that they must reflect wider mass intervals yielding stars of the given colour at a certain time. The explanation for this is that in the vicinity of the turnoff, the isochrones run almost vertically and the colours of stars become nearly independent of mass for a significant range of masses. In Fig. 18 the blue age distribution for $B-V \approx 0.65$ shows eight peaks produced in this way, one from each of the eight metallicities used for the 'thin disk' component and also a low-metallicity feature at high ages. Because the dominant peaks all lie at ages higher than 5 Gyr, they raise the average age of stars in this colour bin above that of the bin for $B-V = 0.91$, which contains only stars too low in mass to have reached the turnoff.

6 CONCLUSION

We have updated the work of DB98 and BDB00 to take advantage of the reworking of the *Hipparcos* catalogue by van Leeuwen (2007), the availability of line-of-sight velocities from the Geneva–Copenhagen survey, and significant improvements to the modelling. The latter include updated isochrones, better treatments of interstellar reddening, the selection function and the age-metallicity relation, and exploration of a wider range of histories of star-formation and stellar acceleration.

We have redetermined the solar motion with respect to the LSR. The new value (eq. 1) is very similar to that of DB98 but has smaller error bars. We have redetermined the structure of the velocity ellipsoid as a function of colour.

Again the results differ from those of DB98 mainly in the reduced error bars.

The most striking change in results compared to BDB00 is an increase in the minimum age of the solar neighbourhood $\tau_{\max}$. This increase is largely due to an improved treatment of interstellar reddening, which was overestimated by BDB00. Models in which the SFR is $\propto \exp(\gamma\tau)$ fit the data best at $\tau_{\max} \approx 12.5$ Gyr and favour $\tau_{\max} > 11.5$ Gyr; these models yield a lower age limit of 10.5 Gyr. Models in which the SFR is a double exponential corresponding to the formation of the thick and thin discs favour ages in the range $10.5 - 12$ Gyr and yield a lower limit of 10.0 Gyr. For either model of the SFR, the lower age limit of BDB00, 9 Gyr, can be excluded. Our estimates are in good agreement with the 12 Gyr age derived by Just & Jahreiss (2007) and the 11.7 Gyr obtained by SB09a. It is also in agreement with the individual stellar ages of GCS and GCS2, which include a significant fraction of ages between 10 and 15 Gyr. The study of Galactic evolution in a cosmological context by Hernandez et al. (2001) yields $\tau_{\max} = 11$ Gyr, while that of Naab & Ostriker (2006) yields $\tau_{\max} \sim 10$ Gyr, our lower limit. Thus there is a considerable body of evidence that the solar neighbourhood started forming a remarkably long time ago.

The strong correlation between the parameters α and γ that characterise the IMF and SFR, which was discussed by Haywood et al. (1997) and BDB00, limit what we can say about the IMF and SFR. We use a Kroupa et al. (1993) IMF and find that the SFR is decreasing: the factor by which it decreases from the beginning of star formation until now is found to lie between ~ 6.5 and ~ 2.5. This conclusion agrees with the findings of Chiappini et al. (1997) and of Just & Jahreiss (2007), who used a non-exponential time dependence of the SFR, and what we find when the SFR is modelled by a sum of exponentials in time.

Our conclusion regarding the time dependence of the SFR conflicts with the finding of BDB00 that the SFR was essentially flat for a Salpeter IMF because the introduction of variable scale heights decreases the visibility of red stars relative to blue stars, so the models have to predict the existence of a higher fraction of red stars than formerly. It also conflicts with the conclusion of SB09a that the SFR is only mildly decreasing for a Salpeter IMF because in their models many of the old stars in the solar neighbourhood are immigrants from smaller radii while immigration of young stars is negligible. Hernandez et al. (2001) conclude that the SFR increases in the first ~ 4 Gyr and then decreases by a factor 2 until now, while Rocha-Pinto et al. (2000) argue that the Milky Way disc has a generally increasing but very irregular SFR. Neither picture is compatible with our results. There are similar conflicts with the conclusions of Bertelli & Nasi (2001) that the SFR is broadly increasing and of Naab & Ostriker (2006) that the SFR increases early on and has been roughly constant over the last ~ 5 Gyr.

We can exclude the scenario of Quillen & Garnett (2000) that disc heating saturates after 3 Gyr but at 9 Gyr the velocity dispersion abruptly increases by a factor of almost 2. However, we are not able to exclude a later saturation of disc heating (after $\gtrsim 4$ Gyr) that is combined with an abrupt increase in dispersion more recently than 9 Gyr ago. Similarly, Seabroke & Gilmore (2007) find that a saturation at $\gtrsim 4.5$ Gyr is not excluded and that there is "extremely tentative" evidence of an abrupt feature in the age-velocity dispersion at 8 Gyr. Nevertheless, nothing in the data calls for early saturation of disc heating, and scenarios that include it yield worse but formally acceptable fits to the data.

Our favoured value $\beta = 0.35$ for the exponent that governs the growth of σ_{total} is in perfect agreement with the findings of GCS (0.34) and BDB00 (0.33). Moreover, the value of GCS3 (0.40) is also still in the range allowed by our models. The classical value of $\frac{1}{2}$ (Wielen 1977) yields rather bad fits and has to be regarded as the very upper limit for β.

For σ_U we find $\beta \approx 0.31$, the same value as in GCS (0.31), but lower than that of GCS3, whose 0.39 is yet not out of range. For σ_V we find $\beta \approx 0.43$, which is higher than the GCS and GCS3 values of 0.34 and 0.40. However, had they not ignored their oldest bins of stars, they would have obtained a larger value for β. For σ_W we find $\beta \approx 0.45$, in good agreement with GCS (0.47) and lower than the value of GCS3 (0.53), but higher than the 0.375 favoured by Just & Jahreiss (2007).

The values and time dependencies of the ratios σ_1/σ_2 and σ_1/σ_3 plotted in Fig. 5 provide important clues to the still controversial mechanism of stellar acceleration. The original proposal (Spitzer & Schwarzschild 1953) was that acceleration is a result of stars scattering off gas clouds. This process leads to characteristic axial ratios of the velocity ellipsoid. Sellwood (2008) has recently redetermined these ratios and finds $\sigma_1/\sigma_2 = 1.41$ and $\sigma_1/\sigma_3 = 1.61$, both of which are smaller than Fig. 5 implies. This result suggests that scattering by spiral arms, which increases σ_1 and σ_2 but not σ_3, plays an important role (Jenkins 1992). Further work is needed to quantify this statement in the light of Sellwood's recent work.

Another indication that scattering by clouds is not alone responsible for acceleration is the finding of Hänninen & Flynn (2002) that in simulations of disc heating by clouds, $\beta = (0.21 \pm 0.02)$, a value that we have excluded. For a disc heated by scattering off a combination of gas clouds and massive black holes in the dark halo Hänninen & Flynn (2002) find $\beta = 0.42$ and $\sigma_1/\sigma_3 = 1.59$, which is excluded by Fig. 5.

It is widely believed that acceleration by spiral arms is responsible for the concentration of solar-neighbourhood stars in the (U, V) plane (Raboud et al. 1998; Dehnen 2000; De Simone et al. 2004). Seabroke & Gilmore (2007) have argued that this concentration undermines the concept of the velocity ellipsoid. However, it remains the case that the velocity dispersions σ_U and σ_V increase systematically with age and it is not evident that any inconsistency arises from modelling this phenomenon as we do here just because spiral structure accelerates stars in groups rather than individually.

SB09a have recently argued that radial mixing plays an important role in disc heating and causes a higher value of β to be measured in the solar neighbourhood than characterises the underlying acceleration process. The origin of this effect is that stars migrate into the solar neighbourhood from small radii where the velocity dispersions are relatively high. Since the fraction of immigrants among the local population increases with stellar age, this effect enhances the velocity dispersion of old stars more than that of young stars, leading to a larger effective value of β. Our value for β_W is in good agreement with the prediction of SB09a for a *Hipparcos* sample.

The models of SB09a are more elaborate than ours not only in that they include radial migration but also in that they include chemical evolution. However, their parameters are determined by fitting to the GCS sample rather than the *Hipparcos* sample employed here. The current sample covers a wider range of colours and is better defined than the GCS sample. Moreover, SB09a made no attempt to match the kinematics of the GCS sample but assumed the validity of the description of the acceleration process given by BDB00; they confined themselves to the metallicity distribution and Hess diagram of the GCS sample. Ideally one would fit simultaneously the local kinematics, metallicity and Hess diagram. However, given the importance of radial migration implied by the studies of Haywood (2008), SB09a and Schönrich & Binney (2009b), such a study would ideally include a more realistic treatment of the integrals of motion than the simple separability of the radial and vertical motions assumed here and by SB09a.

The cosmic SF rate peaked at redshifts $1-2$ (e.g. Ly et al. 2007), which in the concordance cosmology corresponds to look-back times between 7.8 and 10.5 Gyr. These times are $1-2$ Gyr later than the times $\tau_{\rm max}$ at which star formation starts in our models, which is also the time at which the local star-formation rate peaked. It is also slightly later than the mean formation times, $\sim 1.5\pm1$ Gyr, of bulges in a recent series of large simulations of galaxy formation (Scannapieco et al. 2009). On the other hand these authors found that the mean formation times of discs at $R\sim10$ kpc were 4 ± 2 Gyr. The analogous time for the one of our models of the solar neighbourhood is

$$\begin{aligned}\overline{\tau} &= \tau_{\rm H}-\frac{\int_0^{\tau_{\rm max}}{\rm d}t\,t{\rm e}^{\gamma t}}{\int_0^{\tau_{\rm max}}{\rm d}t\,{\rm e}^{\gamma t}}\\ &= \tau_{\rm H}-\tau_{\rm max}+\gamma^{-1}\left(1-\frac{\gamma\tau_{\rm max}}{{\rm e}^{\gamma\tau_{\rm max}}-1}\right). \qquad (21)\end{aligned}$$

The models listed in Table 2 yield values of $\overline{\tau}$ that range between 5.9 Gyr and 6.4 Gyr. These values fall at the upper end of the times obtained by Scannapieco et al. (2009). This overshoot may be connected to the fact that their models have discs that are underweight by almost an order of magnitude; in the models disc formation may be artificially truncated. Thus our results are broadly in agreement with the results of ab-initio simulations of galaxy formation in the concordance cosmology, even though the age of the oldest solar-neighbourhood stars is remarkably large. At least some of these stars will be immigrants from small radii, and if they all are, star-formation will have started later than is implied by our values of $\tau_{\rm max}$. It is currently hard to place a limit on the fraction of the oldest stars that are immigrants because the models of SB09a assume that the disc's scale length does not increase over time, as is likely to be the case.

Thanks to adaptive optics, gas-rich discs, in which stars are forming exceedingly rapidly, can now be studied observationally at $z\simeq2$ (e.g. Genzel et al. 2008), soon after the oldest solar-neighbourhood stars formed. The discs observed are clumpy and highly turbulent, so it seems more likely that they will turn into bulges than a system as dynamically cold as the solar neighbourhood. Nonetheless, studies of these systems bring us tantalisingly close to the goal of tying together studies of 'galactic archaeology' such as ours with observations of galaxies forming in the remote past.

ACKNOWLEDGEMENTS

We thank Gianpaolo Bertelli for providing us with the latest isochrones and valuable comments on their influence on our models and Ralph Schönrich for valuable discussions. MA thanks Merton College Oxford for its hospitality during the academic year 2007/8.

REFERENCES

Bertelli G., Nasi E., 2001, A&A, 121, 1013

Bertelli G., Girardi L., Marigo P., Nasi E., 2008, A&A, 484, 815

Binney J.J., Tremaine S., 2008, *Galactic Dynamics: Second Edition.*, Princeton University Press, Princeton

Binney J.J., Gerhard O., Spergel D., 1997, MNRAS, 288, 365

Binney J.J., Dehnen W., Bertelli G., 2000, MNRAS, 318, 658 (BDB00)

Bensby T., Feltzing S., Lundström I., 2004, A&A, 421, 969

Casagrande L., Flynn C., Portinari L., Girardi L., Jimenez R., 2007, MNRAS, 382, 1516

Chaplin W.J., Serenelli A.M., Basu S., Elsworth Y., New R., Verner G.A., 2007, ApJ, 670, 872

Chiappini C., Matteucci F., Gratton R., 1997, ApJ, 477, 765

Chiappini C., Matteucci F., Romano D., 2001, ApJ, 554, 1044

Crezé M., Chereul E., Bienamé O., 1998, A&A, 340, 384

Dehnen W., 1998, AJ, 115, 2384

Dehnen W., 2000, AJ, 119, 800

Dehnen W., Binney J.J., 1998, MNRAS, 298, 387 (DB98)

De Simone R.S., Wu X., Tremaine S., 2004, MNRAS, 350, 627

Edvardsson B., Andersen J., Gustafsson E., Lambert D.L., Nissen P.E., Tomkin J., 1993, A&A, 275, 101

ESA, 1997, *The Hipparcos and Tycho Catalogues*, ESA-SP 1200

Frisch P.C., 1995, S.S.Rv., 72, 499

Genzel R., et al., 2008, ApJ, 687, 59

Girardi L., Salaris M., 2001, MNRAS, 323, 109

Grevesse N., Asplund M., Sauval A.J., 2007, S.S.Rv., 130, 105

Hakkila J., Myers J.M., Stidham B.J., Hartmann D.H., 1997, AJ, 114, 2043

Hänninen J., Flynn C., 2002, MNRAS, 337, 731

Haywood M., 2001, MNRAS, 325, 1365

Haywood M., 2008, MNRAS, 388, 1175

Haywood M., Robin A.C., *Crézé* M., 1997, A&A, 320, 428

Hernandez X., Avila-Reese V., Firmani C. 2001, MNRAS, 327, 329

Høg E. et al. 2000, A&A, 355, L27

Holmberg J., Nordström B., Andersen J., 2007, A&A, 475, 519 (GCS2)

Holmberg J., Nordström B., Andersen J., 2008, arXiv:0811.3982v1(GCS3)

Jimenez R., Flynn C., MacDonald J., Gibson B.K., 2003, Sci, 299, 1552

Jenkins A., 1992, MNRAS, 257, 620

Joshi Y.C., 2007, MNRAS, 378, 768

Juric M. et al., 2008, ApJ, 673, 864

Just A., Jahreiss H., 2007, arXiv:0706.3850

Kroupa P., Tout C.A., Gilmore G., 1993, MNRAS, 262, 545

Lallement R., Welsh B.Y., Vergely J.L., Crifo F., Sfeir D., 2003, A&A, 411, 447

Ly. C. et al., 2007, ApJ, 657, 738

Naab T., Ostriker J.P., 2006, MNRAS, 366, 899

Nordström B. et al., 2004, A&A, 418, 989 (GCS)

Parenago P.P., 1950, Azh, 27, 150

Persinger T., Castelaz M.W., 1990, AJ, 100, 1621

Press W. H., Flannery B. P., Teukolsky A. A., Vetterling W. T, 1986, *Numerical Recipes.*, Cambridge University Press, New York

Quillen A.C., Garnett R.G., 2000, astro-ph/0004210v3

Raboud D., Grenon M., Martinet L., Fux R., Udry S, 1998, A&A, 335, 61

Rocha-Pinto H., Scalo J., Maciel W.J., Flynn C., 2000, A&A, 358, 869

Scannapieco C., White S.D.M., Springel V., Tissera P.B., 2009, MNRAS, in press

Schönrich R., Binney J.J., 2009, MNRAS, in press, arXiv:0809.3006 (SB09a)

Schönrich R., Binney J.J., 2009, submitted

Seabroke G.M., Gilmore G. , 2007, MNRAS, 380, 1348

Sellwood J.A., 2008, in Funes J.G., Corsini E.M., eds, ASP Conf. Ser. Vol. 396, Formation and Evolution of Galaxy Disks. Astron. Soc. Pac., San Francisco, p. 241

Spergel D.N. et al., 2007, ApJS, 170, 377

Spitzer L., Schwarzschild M., 1953, ApJ, 118, 106

Vergely J.L., Freire Ferrero R., Egret D., Köppen J., 1998, A&A, 340, 543

van Leeuwen F., 2007, *Hipparcos, the New Reduction of the Raw Data*, Springer Dordrecht

Wielen R., 1977, A&A, 60, 263